

Detectability of compact binary merger macronovae

S. Rosswog^{*1}, U. Feindt², O. Korobkin³, M.-R. Wu⁴, J. Sollerman¹, A. Goobar², G. Martinez-Pinedo⁵

¹ *The Oskar Klein Centre, Department of Astronomy, AlbaNova, Stockholm University, SE-106 91 Stockholm, Sweden*

² *The Oskar Klein Centre, Department of Physics, AlbaNova, Stockholm University, SE-106 91 Stockholm, Sweden*

³ *Los Alamos National Laboratory, Los Alamos, NM 87545, USA*

⁴ *Niels Bohr International Academy, Niels Bohr Institute, Blegdamsvej 17, 2100 Copenhagen, Denmark*

⁵ *GSI Helmholtzzentrum für Schwerionenforschung, Planckstr. 1, 64291 Darmstadt, Germany & Institut für Kernphysik (Theoriezentrum), Technische Universität Darmstadt, 64289 Darmstadt, Germany*

Draft version

ABSTRACT

We study the optical and near-infrared luminosities and detectability of radioactively powered electromagnetic transients (‘macronovae’) occurring in the aftermath of binary neutron star and neutron star black hole mergers. We explore the transients that result from the dynamic ejecta and those from different types of wind outflows. Based on full nuclear network simulations we calculate the resulting light curves in different wavelength bands. We scrutinize the robustness of the results by comparing a) two different nuclear reaction networks and b) two macronova models. We explore in particular how sensitive the results are to the production of α -decaying trans-lead nuclei. We compare two frequently used mass models: the Finite-Range Droplet Model (FRDM) and the nuclear mass model of Duflo and Zuker (DZ31).

We find that the abundance of α -decaying trans-lead nuclei has a significant impact on the observability of the resulting macronovae. For example, the DZ31 model yields considerably larger abundances resulting in larger heating rates and thermalization efficiencies and therefore predicts substantially brighter macronova transients. We find that the dynamic ejecta from NSNS models can reach peak K-band magnitudes in excess of -15 while those from NSBH cases can reach beyond -16 . Similar values can be reached by some of our wind models. Several of our models (both wind and dynamic ejecta) yield properties that are similar to the transient that was observed in the aftermath of the short GRB 130603B. We further explore the expected macronova detection frequencies for current and future instruments such as VISTA, ZTF and LSST.

1 INTRODUCTION

The recent, direct detection of gravitational waves (Abbott et al. 2016a) has finally opened the door to the long-awaited era of gravitational wave (GW) astronomy. With a sky localization uncertainty of ~ 600 square degrees for the first event, however, the astronomical environment (e.g. type of galaxy or ambient medium density) in which the black hole (BH) merger took place is essentially unknown. To extract this information, measure the event’s redshift and to constrain the evolutionary channels that lead to the merger in the first place one needs a coincident electromagnetic (EM) signal.

While today the majority of LIGO-detectable sources is believed to be binary black holes, advanced detectors should also be able to observe compact binary systems (Belczynski et al. 2016) that contain at least one neutron star (NS; either NSNS or NSBH; hereafter collectively referred to as compact binary mergers, CBMs). In such mergers neutron star matter is decompressed and ejected into space. Within the ejecta rapid neutron capture (*r*-process) synthesizes a range of heavy elements (Lattimer & Schramm 1974; Eichler et al. 1989; Rosswog et al. 1999; Freiburghaus et al. 1999) up to and beyond the platinum peak near $A=195$. The subsequent

radioactive decay of the freshly synthesized *r*-process elements in the expanding ejecta causes EM transients known as ‘macronovae’ (MN)¹ (Li & Paczyński 1998; Kulkarni 2005; Rosswog 2005; Metzger et al. 2010; Roberts et al. 2011). They are promising EM counterparts of GWs (Metzger & Berger 2012), since they are –contrary to gamma-ray bursts– close to isotropic and viewing angle effects are only of order unity (Grossman et al. 2014). By now, there are three cases where near-infrared excesses in the aftermath of gamma-ray bursts have been interpreted as being due to macronovae (Tanvir et al. 2013; Berger et al. 2013; Jin et al. 2015; Yang et al. 2015).

CBMs eject matter via several channels, see Fig. 1 and e.g. Fernandez & Metzger (2015) and Rosswog (2015c) for recent reviews. The best-studied channel (stage ‘II’ in Fig. 1) is the so-called *dynamic ejecta* (Rosswog et al. 1999; Ruffert & Janka 2001; Oechslin et al. 2007; Bauswein et al. 2013; Hotokezaka et al. 2013;

¹ The same phenomenon is often referred to as ‘kilonova’. We prefer ‘macronova’ (MN), since the phenomenon is *not* a thousand times brighter than a nova, as originally thought. See Metzger (2016) for discussion of the naming conventions.

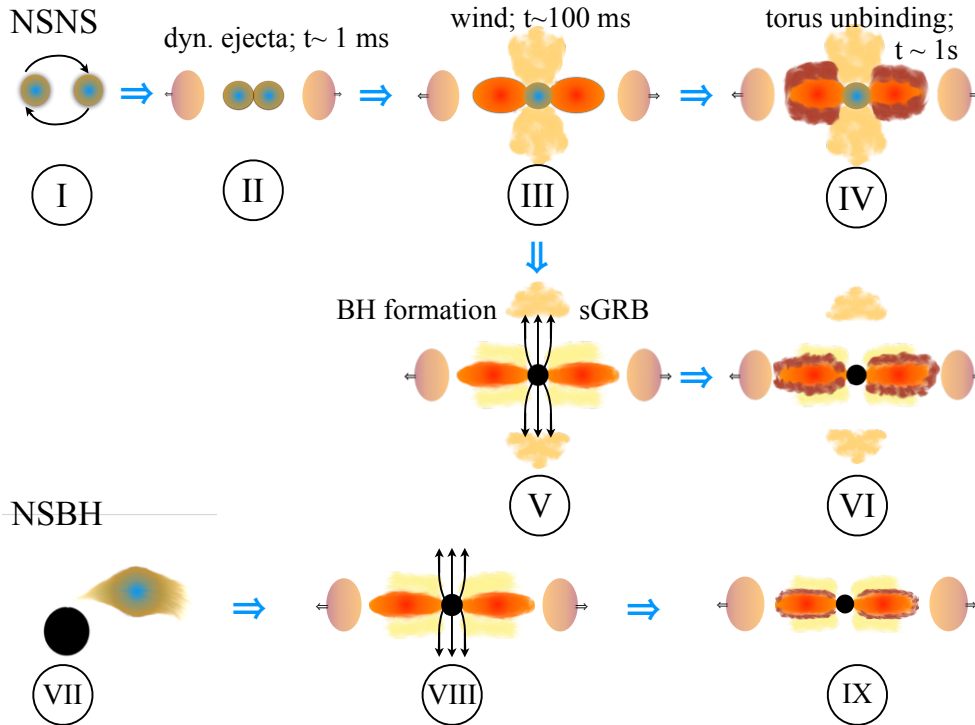


Figure 1. Overview of the different mass loss channels in both the NSNS and NSBH case.

Rosswog 2013; Lehner et al. 2016) that become unbound immediately at merger. They are launched by either gravitational torques (“tidal component”) or, in the NSNS case, by hydrodynamic interaction at the interface between the stars (“interaction component”, see Oechslin et al. (2007) and Korobkin et al. (2012)²). While the tidal component carries away matter with the original, very low electron fraction ($Y_e \approx 0.04$) which is set by cold β -equilibrium in the original neutron star, the interaction component is heated and can increase its Y_e via positron captures $e^+ + n \rightarrow p + \bar{\nu}_e$. Both sub-components, however, share the property that they are hardly impacted by neutrino irradiation (see e.g. Radice et al. 2016), simply because they have already reached large distances from the remnant before the neutrino luminosity starts rising in earnest (after accretion torus formation at $t > 10$ ms after contact). Nevertheless, for material that is not immediately ejected, weak interactions can change the electron fraction substantially, see e.g. Wanajo et al. (2014) who find a particularly large fraction of high Y_e material in the ejecta.

The dynamically ejected matter is complemented by baryonic winds that are driven by neutrino-energy deposition, magnetic fields, viscous evolution and/or nuclear recombination energy (Beloborodov 2008; Metzger et al. 2008; Dessart et al. 2009; Fernandez & Metzger 2013a; Perego et al. 2014; Siegel et al. 2014; Just et al. 2015; Ciolfi & Siegel 2015; Martin et al. 2015). If a completely or temporarily stable neutron star survives in the centre of a merger remnant (see stage “III” in Fig. 1) the neutrino- and the magnetically driven winds are substantially enhanced in comparison to the case where a BH forms immediately. Simulations indicate that a prompt collapse of the massive neutron star to a black hole can be avoided in many cases (Baumgarte et al. 2000; Kaplan

et al. 2014; Kastaun & Galeazzi 2015; Takami et al. 2014; Gondek-Rosinska et al. 2016) even if the central mass substantially exceeds the Tolman-Oppenheimer-Volkoff (TOV) limit. The calculations of Shibata & Taniguchi (2006) and Hotokezaka et al. (2011, 2013) indicate that prompt collapse is avoided, unless the initial mass of the binary exceeds the TOV mass limit by more than $\sim 35\%$. The two precisely determined neutron star masses near $2.0 M_\odot$ (J1614-2230, Demorest et al. (2010) and PSR J0348+0342, Antoniadis et al. (2013)), place this threshold value to at least $2.7 M_\odot$. Thus, a large fraction of the mergers may go through such a metastable phase with a strong neutrino-driven wind phase and binaries at the low mass end may even produce stable, very massive neutron stars. Recent studies (Murguía-Berthier et al. 2014, 2016) indicate, however, that a BH needs to form on a time scale of less than ~ 100 ms in order to launch a short GRB (stage “V” in Fig. 1), otherwise outflows will be baryon-overloaded and will not reach relativistic speeds. Seconds after the burst the resulting BH-disk system can release a good fraction of its disk (stage “VI”). Recent work (Fernandez & Metzger 2013a; Just et al. 2015) suggests that neutrinos play a sub-dominant role for the mass loss once a BH has formed. NSBH mergers (stage “VII”) can release substantially more matter in dynamic ejecta than NSNS binaries (Rosswog 2005; Duez et al. 2010; Deaton et al. 2013; Foucart et al. 2013; Kyutoku et al. 2013; Foucart et al. 2014; Bauswein et al. 2014). If a sufficiently massive torus forms around the BH, it is expected that a jet can be launched into a relatively unpolluted surrounding (stage “VIII”). But large BH-masses in combination with low spins may lead to very small or no disks (Foucart 2012; Rosswog 2015c). On longer times scales a fair fraction of the initial disk mass is expected to become unbound (stage “IX”), just as in the NSNS case.

Recently, a fast neutron component has been claimed to produce a macronova precursor signal (Metzger et al. 2015). This model is based on SPH simulations in the conformal flatness approximation

² See Fig. 2 in the latter publication for an illustration.

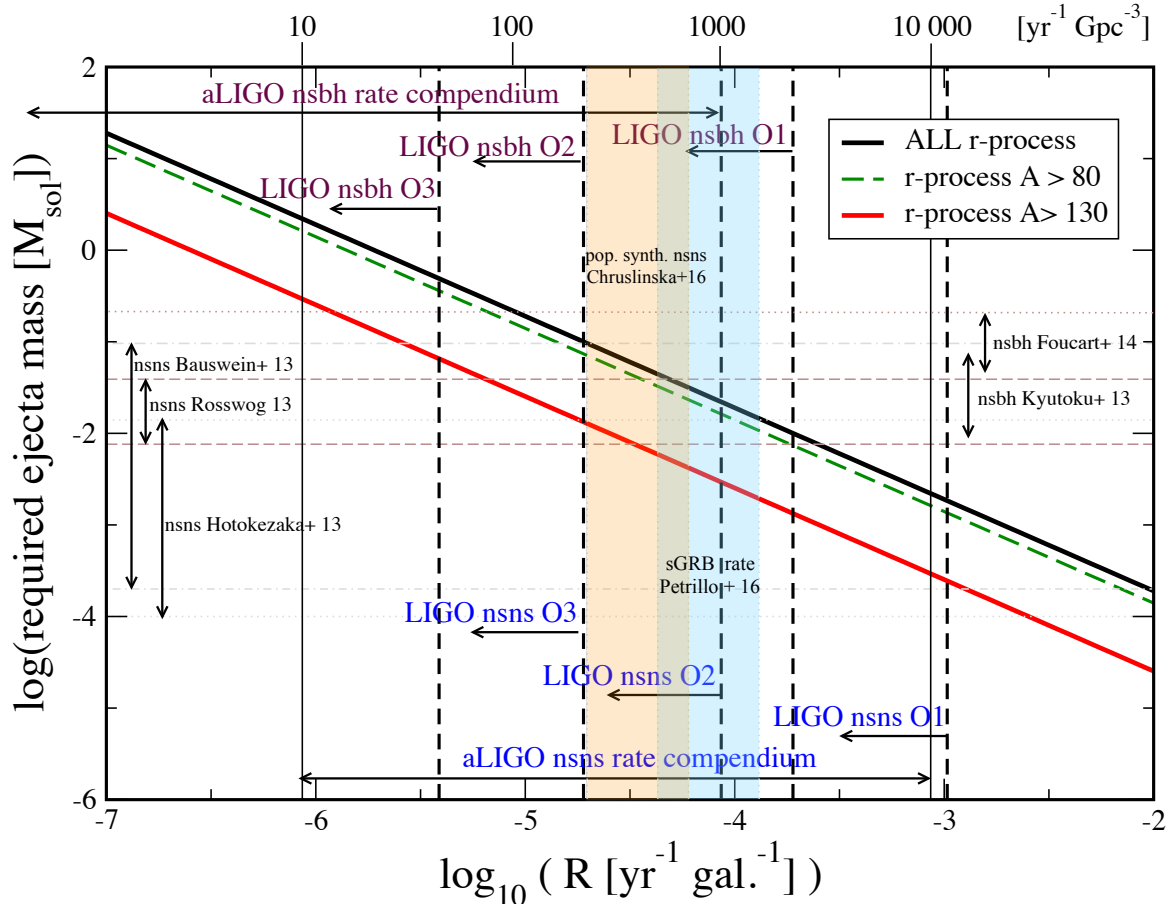


Figure 2. Summary of various rate constraints. The lines from the upper left to lower right indicate the typical ejecta mass required to explain all r-process/all r-process with $A > 80$ /all r-process with $A > 130$ for a given event rate (lower panel per year and Milky Way-type galaxy, upper panel per year and Gpc^3). Also marked is the compiled rate range from Abadie et al. (2010) for both double neutron stars and neutron star black hole systems and (expected) LIGO upper limits for O1 to O3 (Abbott et al. 2016b). The dynamic ejecta results from some hydrodynamic simulations are also indicated.

where a few particles are ejected early on with a high velocity from the shear interface between the two merging neutron stars. While such a precursor is a possibility, we do not see it in our simulations and neither do, e.g., Lehner et al. (2016) in their recent GR simulations. Therefore, we will not consider this possibility in the following discussion.

Our knowledge of the rates of compact binary mergers is still plagued by large uncertainties. Simple constraints can be derived by assuming that they are related to the production of r-process elements. If we take the solar-system r-process abundance pattern (Arnould et al. 2007) as representative and define a quantity $\sigma(A) = \sum_{A_i > A} X_{A_i}^r$, where $X_{A_i}^r$ is the r-process mass fraction with nucleon number A_i and use a baryonic mass of $M_{b, \text{MW}} = 6 \times 10^{11} M_{\odot}$ (McMillan 2011), we find that the Milky Way contains $\approx 19000 M_{\odot}$ of r-process material in total. About $M_{r, > 130} = \sigma(130)M_{b, \text{MW}} = 2530 M_{\odot}$ of this matter has $A > 130$ and about $500 M_{\odot}$ are beyond the “platinum peak” ($A \geq 195$). With an age of the Galaxy of $\tau_{\text{MW}} \approx 10^{10}$ yrs, this yields average production rates of $\dot{M}_{r, \text{all}} = 1.9 \times 10^{-6} M_{\odot} \text{ yr}^{-1}$, $\dot{M}_{r, A > 130} = 2.5 \times 10^{-7} M_{\odot} \text{ yr}^{-1}$ and $\dot{M}_{r, A > 195} = 5 \times 10^{-8} M_{\odot} \text{ yr}^{-1}$. The product of average ejecta mass and event rate is known but the individual factors are not. This is shown as lines from the upper left to the lower right in Fig. 2 (e.g.

r-process with $A > 130$ in red). As an example, if an event that produces all r-process $A > 130$ occurs at a rate of 10^{-5} yr^{-1} it has to eject $2.5 \times 10^{-2} M_{\odot}$ each time. For comparison, some representative simulation results for both NSNS (Hotokezaka et al. 2013; Bauswein et al. 2013; Rosswog 2013) and NSBH (Kyutoku et al. 2013; Foucart et al. 2014) are also indicated. We also translated the rates from $\text{yr}^{-1} \text{ MWEG}^{-1}$ (bottom axis) to $\text{yr}^{-1} \text{ Gpc}^{-3}$ (axis on top) via a density of $1.16 \times 10^{-2} \text{ MWEG Mpc}^{-3}$ (Abadie et al. 2010). Here MWEG abbreviates “Milky Way equivalent galaxy”. Also indicated are the expected LIGO upper limits of science runs O1-O3 (Abbott et al. 2016b). We have further marked the NSNS merger rates from the population synthesis studies of Chruslinska et al. (2016) and the range of sGRB rates estimated by Petrillo et al. (2013).

The paper is organized as follows. In Sec. 2 we describe the methodological elements that enter our study. We discuss in particular our hydrodynamic simulations, the used nuclear reaction networks and our two macronova models. Section 3 presents our results on nucleosynthesis and discusses the impact of different nuclear mass formulae on the resulting abundances, the thermalization efficiency and the radioactive heating rates. We further present optical and near-infrared lightcurves and we discuss the detection

feasibility, the follow-up of LIGO triggers and the use of GRB-triggers to search for macronovae. Sec. 4 summarizes the main findings of this study.

2 METHODOLOGY

In this study we explore macronova transients based on nuclear network calculations along thermodynamic trajectories. We perform a set of hydrodynamic simulations to obtain trajectories for dynamic NSNS ejecta, for other cases we use a parametrized treatment with numerical values based on existing hydrodynamic studies.

2.1 NSNS merger simulations

The simulations performed for this study make use of the Smooth Particle Hydrodynamics method (SPH) (Monaghan 2005; Rosswog 2009; Springel 2010; Price 2012; Rosswog 2015b) coupled with a temperature-dependent nuclear equation of state (Shen et al. 1998) and an opacity-dependent multi-flavour neutrino leakage scheme (Rosswog & Liebendörfer 2003). This treatment includes in particular electron and positron captures and therefore the nuclear matter can change its electron fraction Y_e in the course of the merger. A concise summary of the implemented physics and of our numerical techniques can be found in Rosswog et al. (2013). The only noticeable change is that we are using the Wendland C6 kernel (Wendland 1995; Schaback & Wendland 2006) together with 200 neighbours per particle. We have recently scrutinized various ingredients in the SPH method (Rosswog 2015a) and found that this kernel has excellent numerical properties and in particular drastically reduces the noise in an SPH simulation in comparison to the cubic spline kernel that is commonly used. The binary systems that are explored are summarized in Table 1, each of them is modeled with 10^6 SPH particles and the stars have negligible initial spin as expected in nature due to the very short tidal interaction time and the low viscosity of neutron star matter (Bildsten & Cutler 1992; Kochanek 1992). Our typical simulation time is ~ 30 ms. As an example, a series of snapshots from a NSNS simulation (1.3-1.3 M_\odot ; run N2; color-coded is the electron fraction Y_e) is shown in Fig. 3.

2.2 Ejecta

We identify unbound matter in our hydrodynamic simulations by the criterion $v_a^2/2 + \phi_a > 0$ at the end of our simulation, where a labels the SPH particle and v and ϕ are velocity and gravitational potential. To double-check this criterion we compare with a criterion based on the outward radial velocity being larger than the local escape velocity. The ejecta masses based on both criteria agree with each other to within $\sim 2\%$. To have a robust upper limit, we also examine $v_a^2/2 + \phi_a + u_a > 0$, where u_a is the specific internal energy of a particle a . The resulting mass is noted as $m_{ej,max}$ in Table 1, and it is used to set the upper limit that can be plausibly expected for the electromagnetic signal from dynamic ejecta.

Studies that focus on the long-term evolution of accretion disks around BHs (Wanajo & Janka 2012; Fernandez & Metzger 2013b,a; Just et al. 2015; Wu et al. 2016) find that a substantial fraction ($\sim 20\%$) of the initial torus can become unbound. According to Giacomazzo et al. (2013) the torus masses can, depending on the initial mass ratio, be very large and reach multiples of 0.1 M_\odot . Thus the unbound mass from accretion tori can be large and actually rival the dynamic ejecta masses of even asymmetric mass ratio NSNS/NSBH mergers. The exploratory numerical studies, how-

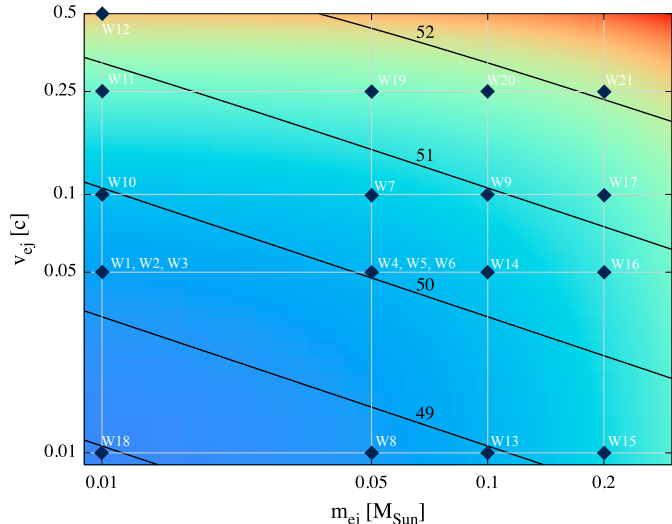


Figure 4. Explored parameter space for the parametric wind studies (different winds are annotated, e.g., as “W1” for wind 1). For the corresponding parameters are summarized in Tab. 2. The black lines indicate the kinetic energy in the winds with the line labeled “50”, for example, indicating 10^{50} erg.

ever, suggest that the velocities are substantially lower than in the dynamic ejecta case. Just et al. (2015), for example, find that the average velocities of the torus component never exceed 0.06 c , while the dynamic ejecta in the NSBH cases can be larger than 0.2 c , see Table 1.

We subsume all the ejecta types other than dynamic ejecta under the broad category “winds”. Despite their different origin, they all have in common that they are exposed for longer time to the neutrino irradiation, therefore this material has a larger Y_e and consequently a different nucleosynthesis. In particular, such matter has a lower content in those elements that are the major opacity sources (Kasen et al. 2013; Tanaka & Hotokezaka 2013; Fontes et al. 2015). With potentially different nuclear heating rates and lower opacities, these winds are promising sources for EM transients, that could potentially outshine the signals from the dynamic ejecta, if they are not obscured by them. A first study by Fernandez et al. (2015) finds, however, that due to their different velocities, the wind expansion at large radii is not influenced by the dynamic ejecta.

Our parametric wind model contains four parameters: the wind mass m_w , the initial entropy s_0 , the electron fraction Y_e and the (terminal) wind velocity v_w . To create initial conditions for the network and subsequent macronova calculations, we also need a starting temperature T_0 and an initial radius R_0 . The starting temperature is chosen as $T_0 = 9 \times 10^9$ K, so that we are safely above the threshold temperature for nuclear statistical equilibrium (NSE, $T_{NSE} \approx 5 \times 10^9$ K). Thus, the initial abundance distribution is set by NSE and, below 8×10^9 K, the nuclear reaction network takes over. The initial radius R_0 is found by the requirement that the average density $\rho_0 = 3m_w/(4\pi R_0^3)$ together with T_0 reproduces the desired initial entropy s_0 . To keep the parameter space under control and motivated by the strongly peaked entropy distribution of Perego et al. (2014, their Fig. 7), Just et al. (2015) and Fernandez et al. (2015), we fix the initial entropy to values of 15 k_B per baryon. Typical values for R_0 are ~ 650 km, in reasonable agreement with the numerical studies of neutrino-driven winds

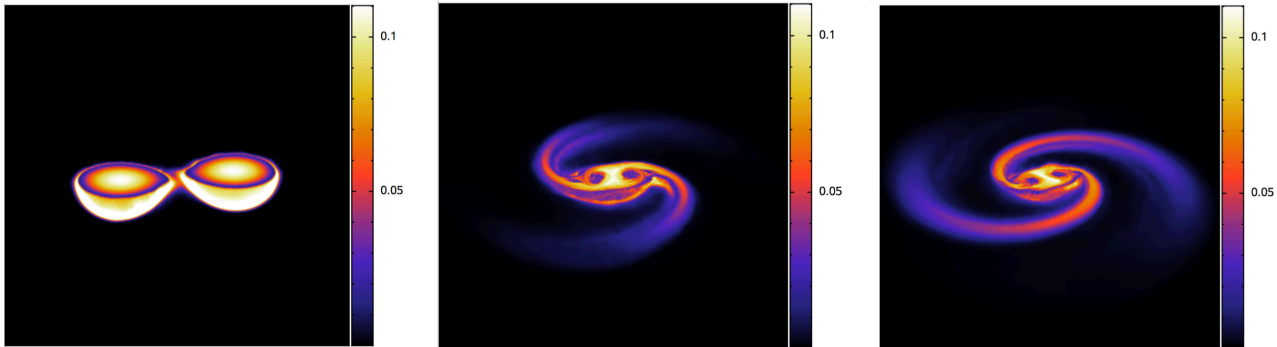


Figure 3. Electron fraction in a 1.3-1.3 M_{\odot} merger (model N2; only matter below orbital plane shown) at $t=7.06, 11.6$ and 12.4 ms.

Table 1. Overview over the simulation parameters. Also shown are the resulting mass fractions of lanthanide (X_{lan}) and actinide (X_{act}) elements. All NSBH cases start with an initial entropy of $2 k_B/\text{nuc}$ and $Y_e=0.06$.

Dynamic ejecta NSNS mergers

Run	$m_1 [M_{\odot}]$	$m_2 [M_{\odot}]$	$t_{\text{end}} [\text{ms}]$	$m_{\text{ej}} [10^{-2} M_{\odot}]$	$\langle v_{\text{ej},\infty} \rangle [c]$	$m_{\text{ej,max}} [10^{-2} M_{\odot}]$	$X_{\text{lan}} [10^{-2}]$	$X_{\text{act}} [10^{-2}]$
N1	1.2	1.2	32.1	0.79	0.12	3.17	17.22	5.06
N2	1.3	1.3	31.1	1.26	0.11	2.70	17.01	5.69
N3	1.4	1.4	38.3	0.84	0.11	2.25	17.93	6.03
N4	1.2	1.4	30.6	1.59	0.11	2.92	17.82	5.39
N5	1.4	1.8	25.3	3.40	0.12	4.76	16.90	7.57

Dynamic ejecta NSBH mergers

Run	$m_{\text{ns}} [M_{\odot}]$	$m_{\text{bh}} [M_{\odot}]$	χ	$m_{\text{ej}} [10^{-2} M_{\odot}]$	$\langle v_{\text{ej},\infty} \rangle [c]$	$X_{\text{lan}} [10^{-2}]$	$X_{\text{act}} [10^{-2}]$	comment
B1	1.4	7.0	0.7	4.0	0.20	19.87	4.10	Foucart et al. (2014), run M14-7-S7
B2	1.4	7.0	0.9	7.0	0.18	19.27	4.83	Foucart et al. (2014), run M14-7-S9
B3	1.2	7.0	0.9	16.0	0.25	19.48	4.64	Foucart et al. (2014), run M14-7-S9

(Dessart et al. 2009; Perego et al. 2014). Since we are interested here in exploring the lower opacity case, we restrict our study to electron fractions above the threshold value for heavy r-process, $Y_{e,\text{thresh}} = 0.25$ (see Korobkin et al. 2012, their Fig. 8). From the results shown in Perego et al. (2014), we expect terminal wind velocities around $0.05 c$. These numbers motivate our “wind 1” simulation. Once the parameters have been set, the density evolves according to $\rho(t) = \rho_0(1 + v_w t/R_0)^{-3}$ and the temperature evolution is calculated using the HELMHOLTZ equation of state (Timmes & Swesty 2000) according to the entropy change from nuclear reactions (Freiburghaus et al. 1999). The explored wind parameters are given in Tab. 2 and visualized in Fig. 4.

2.3 Nucleosynthesis calculations

For each simulation we perform a nucleosynthesis calculation to obtain the final abundance pattern and the nuclear heating rate $\dot{\epsilon}_{\text{nuc}}$ that is needed for the macronova models. We calculate an average out of 1000 randomly chosen hydrodynamic ejecta trajectories for each of our merger simulations (N1 - N5). Since there is little variation between individual trajectories this is a fair representation of

the overall ejecta dynamics. These average trajectories are used in the network calculations to obtain the nuclear energy generation rate $\dot{\epsilon}_{\text{nuc}}$ that is used in the macronova calculation. For the dynamic ejecta in the NSBH cases (run B1 - B3) and the winds we use the above described expansion model. For the NSBH cases we apply the parameters from the simulations of Foucart et al. (2014). For the entropy and electron fraction they provide results for individual trajectories that are near $Y_e = 0.06$ and $s = 2 k_B/\text{nuc}$. We choose these values in our models, but stress that the nucleosynthesis (and therefore the macronovae) in this regime is insensitive to the exact numbers³. The parameters for the dynamic ejecta are summarized in Table 1. Since what we subsume under “winds” can have different physical origins, see the discussion above, we vary the wind parameters in a wide range, see Table 2.

Our baseline nucleosynthesis calculations are performed with a large nuclear reaction network WinNet (Winteler 2012; Winteler et al. 2012) that is based on the BasNet network (Thielemann et al. 2011). It includes 5831 isotopes from nucleons up to $Z = 111$ be-

³ To illustrate this, have a look at Fig. 8 in Korobkin et al. (2012): *all* trajectories with $Y_e < 0.15$ yield practically identical nucleosynthesis results.

Parametrized winds

run	$m_W [M_\odot]$	Y_e	$v_{w,\infty} [c]$	$E_{\text{kin}} [\text{erg}]$	X_{lan}	X_{act}	comment
wind 1	0.01	0.30	0.05	2.2×10^{49}	1.61×10^{-7}	$< 10^{-15}$	insp. by Perego et al. (2014)
wind 2	0.01	0.25	0.05	2.2×10^{49}	6.30×10^{-5}	$< 10^{-15}$	insp. by Perego et al. (2014)
wind 3	0.01	0.35	0.05	2.2×10^{49}	$< 10^{-15}$	$< 10^{-15}$	insp. by Perego et al. (2014)
wind 4	0.05	0.25	0.05	1.1×10^{50}	2.41×10^{-4}	$< 10^{-15}$	unb. disk material
wind 5	0.05	0.30	0.05	1.1×10^{50}	2.45×10^{-7}	$< 10^{-15}$	unb. disk material; low-viscosity
wind 6	0.05	0.35	0.05	1.1×10^{50}	$< 10^{-15}$	$< 10^{-15}$	unb. disk material; low-viscosity
wind 7	0.05	0.25	0.10	4.5×10^{50}	4.28×10^{-5}	$< 10^{-15}$	
wind 8	0.05	0.30	0.01	4.5×10^{48}	1.57×10^{-4}	$< 10^{-15}$	
wind 9	0.10	0.25	0.10	9.0×10^{50}	7.70×10^{-5}	$< 10^{-15}$	
wind 10	0.01	0.25	0.10	9.0×10^{49}	3.49×10^{-5}	$< 10^{-15}$	
wind 11	0.01	0.25	0.25	5.9×10^{50}	2.13×10^{-2}	6.34×10^{-6}	
wind 12	0.01	0.25	0.50	2.8×10^{51}	7.50×10^{-2}	1.66×10^{-3}	
wind 13	0.10	0.35	0.01	8.9×10^{48}	$< 10^{-15}$	$< 10^{-15}$	
wind 14	0.10	0.30	0.05	2.3×10^{50}	1.35×10^{-7}	$< 10^{-15}$	
wind 15	0.20	0.35	0.01	1.8×10^{49}	$< 10^{-15}$	$< 10^{-15}$	
wind 16	0.20	0.30	0.05	4.5×10^{50}	8.39×10^{-8}	$< 10^{-15}$	
wind 17	0.20	0.25	0.10	1.8×10^{51}	1.27×10^{-4}	$< 10^{-15}$	
wind 18	0.01	0.35	0.01	8.9×10^{47}	$< 10^{-15}$	$< 10^{-15}$	
wind 19	0.05	0.25	0.25	2.9×10^{51}	3.91×10^{-4}	$< 10^{-15}$	
wind 20	0.10	0.25	0.25	5.8×10^{51}	4.95×10^{-5}	$< 10^{-15}$	
wind 21	0.20	0.25	0.25	1.1×10^{52}	3.20×10^{-5}	$< 10^{-15}$	

Table 2. Parameters of the wind models. In all cases a specific entropy of 15 k_B /nucleon is used, X_{lan} is the mass fraction in lanthanides.

tween the neutron drip line and stability. The reaction rates are from the compilation of Rauscher & Thielemann (2000) for the finite range droplet model (FRDM) (Möller et al. 1995) and the weak interaction rates (electron/positron captures and β -decays) are from Fuller et al. (1982) and Langanke & Martinez-Pinedo (2001). In addition, the distribution of fission fragments from Kodama & Takahashi (1975) is used as a default. Finally, we adopt neutron capture and neutron-induced fission rates of Panov et al. (2010) and β -delayed fission probabilities of Panov et al. (2005).

The nucleosynthesis in the dynamic ejecta has been found to be extremely robust against variations of astrophysical parameters (Korobkin et al. 2012), but the final abundance patterns are still sensitive to variations of the nuclear physics such as fission distributions, beta-decay rates and nuclear mass formulae (Mendoza-Temis et al. 2015; Eichler et al. 2015; Goriely 2015; Barnes et al. 2016; Wu et al. 2016; Mumpower et al. 2016). For the dynamic ejecta we explore the impact of the nuclear mass model on the nuclear heating rate. Specifically, we compare the 31-parameter Duflo-Zuker (DZ31) mass formula (Duflo & Zuker 1995) with the Finite Range Droplet Model (FRDM; Möller et al. 1995). The major effect in our context is a substantially enhanced trans-lead nuclei fraction for the DZ31-case, which leads to an increased nuclear heating rate via α -decays (Barnes et al. 2016). These comparisons are performed with the network described in detail in Mendoza-Temis et al. (2015). It includes 7360 nuclei between the proton and neutron drip-lines up to charge number $Z = 110$. For the nuclear masses we use experimental values from the Atomic Mass Evaluation Wang et al. (2012) whenever available. Where available, we use experimental alpha, beta decay and spontaneous fission rates from the NUBASE (Audi et al. 2012) and NuDat2 databases (<http://www.nndc.bnl.gov/nudat2/>) and theoretical predictions otherwise. For the most relevant theoretical rates for the r-process, we employ the beta-decay rates of Moller et al. (2003), the neutron-

capture and the reverse photo-dissociation rates of Mendoza-Temis et al. (2015) for nuclei with $Z \leq 83$ for different mass models, the neutron-capture and neutron-induced fission rates of Panov et al. (2010) for $Z > 83$ with FRDM mass model and Thomas-Fermi fission barriers, and the beta-delayed and spontaneous fission rates of Petermann et al. (2012). The fission fragment distributions are taken from Zinner (2007) calculated by the ABLA code, which well reproduces available fission data and includes the possibility of neutron emission before and after fission.

2.4 Macronovae

2.4.1 Scaling relations

The luminosity of a MN rises as more material becomes visible and once all parts are transparent, one sees a decline in the luminosity dictated by the nuclear energy generation rate, $L \propto \dot{\epsilon}_{\text{nuc}} m_{\text{ej}}$. As a guidance for the following discussion, we provide the scaling laws that follow from simple arguments. After the neutron captures have ceased (~ 1 s after merger) the heating rate can to a reasonable approximation be described by a power law, $\dot{\epsilon}_{\text{nuc}} \propto t^{-\alpha}$, with a power law index $\alpha \approx 1.3$ (Metzger et al. 2010; Roberts et al. 2011; Korobkin et al. 2012; Hotokezaka et al. 2016). The peak emission is reached when expansion and diffusion times are comparable which yields (Grossman et al. 2014)

$$t_{\text{peak}} \approx 4.9 \text{d} \left(\frac{\kappa}{10 \text{ cm}^2/\text{g}} \frac{m_{\text{ej}}}{0.01 M_\odot} \frac{0.1 c}{v_{\text{ej},\infty}} \right)^{1/2} \quad (1)$$

for the peak time,

$$L_{\text{peak}} \approx 2.5 \times 10^{40} \frac{\text{erg}}{\text{s}} \left(\frac{v_{\text{ej},\infty}}{0.1 c} \frac{10 \text{ cm}^2/\text{g}}{\kappa} \right)^{0.65} \left(\frac{m_{\text{ej}}}{0.01 M_\odot} \right)^{0.35} \quad (2)$$

for the bolometric luminosity and

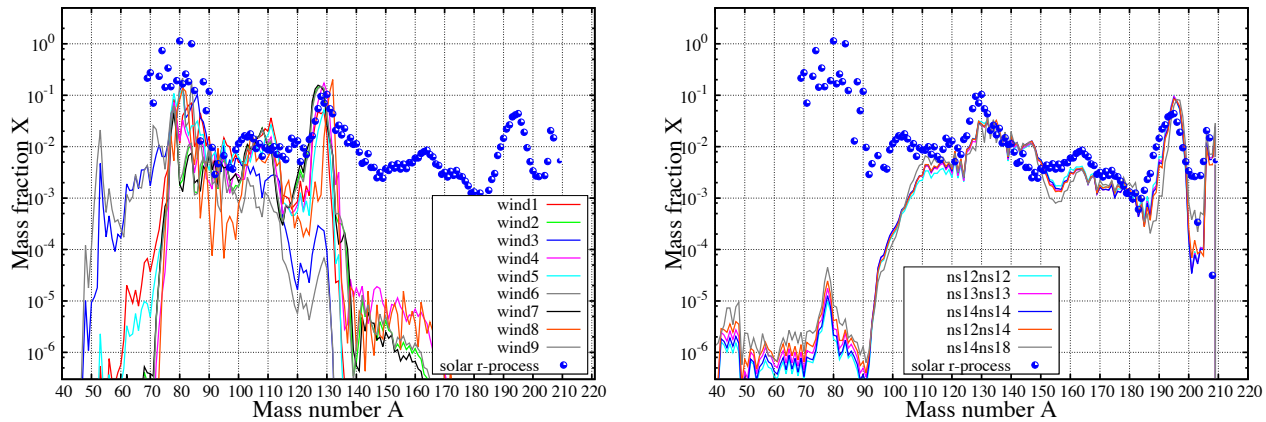


Figure 5. Resulting element distribution for the wind models (left) and dynamic ejecta (right). The blue dots are the solar system r-process mass fractions.

$$T_{\text{eff}} \approx 2200 \text{ K} \left(\frac{10 \text{ cm}^2/\text{g}}{\kappa} \right)^{0.4125} \left(\frac{0.1 c}{v_{ej,\infty}} \right)^{0.0875} \left(\frac{0.01 M_{\odot}}{m_{ej}} \right)^{0.1615} \quad (3)$$

for the effective temperature where all exponents were evaluated with $\alpha = 1.3$.

2.4.2 Model 1

As our macronova model 1 (hereafter ‘MNmodel1’) we employ a model similar to the one used in Grossman et al. (2014) with a spherically symmetric homologously expanding radial density profile $\rho(v) \sim \rho_0(1 - v^2/v_{max}^2)^3$. In this model, it is assumed that all macronova energy originates from the layer above the so-called diffusion surface, defined as the surface for which the average diffusion time is equal to the time from the merger. Any photons traveling below this diffusion surface are considered trapped and therefore invisible. The total luminosity is then taken to be the mass of this layer times the instantaneous radioactive nuclear heating rate; thermal emission from the layer is assumed to be lost to PdV expansion work and therefore neglected. In this sense, our model provides a conservative lower bound for the macronova emission. The emitted spectrum has an effective temperature of the photosphere at optical depth $\tau_{\text{ph}} = 2/3$.

Practically, the models inherit from the hydrodynamic calculation the ejecta mass, the electron fraction and velocity and from the network calculation the instantaneous nuclear heating rate $\dot{\epsilon}_{\text{nuc}}(t)$, assuming that a fixed fraction ($f_{\text{tot}} = 0.5 = \text{const}$) thermalizes at all times while the rest is lost. Note that in model 1 we always use the FRDM mass model (Möller et al. 1995).

A major uncertainty in the prediction of macronova transients are the opacities of the expanding r-process material, which unfortunately has the largest effect on the spectral energy distribution (SED), see Eq. (3). Based on atomic structure models, Kasen et al. (2013) argued that the opacity of expanding r-process material is dominated by bound-bound-transitions from those ions that have

the most complex valence electron structure. They found in particular that even small amounts lanthanides have a large impact on the opacities. For example, the neodymium opacities exceed those of iron as long as their mass fraction $X_{\text{Nd}} > 10^{-4}$. From their studies based on four species, they conclude that a gray opacity of $\approx 10 \text{ cm}^2/\text{g}$ should be fairly effective for calculating bolometric light curves. Similar conclusions were reached in a study by Tanaka & Hotokezaka (2013). However, Kasen et al. (2013) and, more recently, Fontes et al. (2015) point out that even this may be an underestimate, and that the true value could even be an order of magnitude larger.

We use the sum of lanthanide and actinide fraction, $X_{\text{lan}} + X_{\text{act}}$, to decide which opacity value to use. Whenever it exceeds a limiting value of 10^{-3} , we use as fiducial value for the opacity in the dynamic ejecta a value of $\kappa = 10 \text{ cm}^2/\text{g}$, otherwise we use $\kappa = 1 \text{ cm}^2/\text{g}$. The dynamic ejecta show a very large lanthanide fraction of $X_{\text{lan}} \approx 0.18$ while this value varies widely for the different wind cases, see column seven in Table 2, but is in almost all cases below the threshold value.

Since the current knowledge is based on expensive atomic structure calculations of so far only a few ions, the opacity value for strongly lanthanide-enriched material is likely subject to considerable uncertainties. We therefore also explore how our brightest case, N3 with DZ31-mass model, would appear in the case of a substantially larger opacity value ($\kappa = 100 \text{ cm}^2/\text{g}$).

2.4.3 Model 2

A major difference in macronova model 2 (‘MNmodel2’) is that we use time-dependent thermalization efficiencies. In addition, we can switch between the FRDM and the DZ31 nuclear mass model. All MNmodel2 calculations are performed with the Mendoza-Temis et al. (2015) network. The effect of the DZ31 mass model is that a larger fraction of trans-lead nuclei are produced and, as shown below, this has a substantial impact on the nuclear heating rate at times

around and after the macronova peak ($t > 1$ day). The thermalization efficiencies have been explored in recent work (Hotokezaka et al. 2016; Barnes et al. 2016). We apply here the thermalization efficiencies based on simple analytical estimates from the latter work. The thermalization efficiency for photons is estimated as

$$f_\gamma(t) = 1 - \exp\left(-\frac{1}{\eta_\gamma^2}\right), \quad (4)$$

while for the massive particles (electrons, α -particles and fission products) it reads

$$f_i(t) = \frac{\ln(1 + 2\eta_i^2)}{2\eta_i^2}. \quad (5)$$

The quantity η is the ratio of time after the merger and the thermalization time scale of the considered particle, $\eta_k = t/\tau_k$. We use for the different thermalization time scales

$$\tau_\gamma = 1.40 m_5^{1/2} v_2^{-1} \text{ days} \quad (6)$$

$$\tau_e = 7.40 m_5^{1/2} v_2^{-3/2} \left(\frac{0.5 \text{ MeV}}{E_e}\right)^{1/2} \text{ days} \quad (7)$$

$$\tau_\alpha = 7.74 m_5^{1/2} v_2^{-3/2} \left(\frac{6.0 \text{ MeV}}{E_\alpha}\right)^{1/2} \text{ days} \quad (8)$$

$$\tau_{\text{fis}} = 16.77 m_5^{1/2} v_2^{-3/2} \left(\frac{125.0 \text{ MeV}}{E_{\text{fis}}}\right)^{1/2} \text{ days}, \quad (9)$$

where $m_5 \equiv m_{\text{ej}}/(5 \times 10^{-3} M_\odot)$ and $v_2 \equiv v_{\text{ej}}/(0.2c)$. In the following, we evaluate the time scales τ_k at the characteristic scaling energies given above. The total thermalization efficiency is then given by

$$f_{\text{tot}}(t) = \frac{\dot{\epsilon}_\beta(t) [\zeta_\gamma f_\gamma(t) + \zeta_e f_e(t)] + \dot{\epsilon}_\alpha(t) f_\alpha(t) + \dot{\epsilon}_{\text{fis}}(t) f_{\text{fis}}(t)}{\dot{\epsilon}_\beta(t) + \dot{\epsilon}_\alpha(t) + \dot{\epsilon}_{\text{fis}}(t)}, \quad (10)$$

where we use $\zeta_\gamma = 0.45$ and $\zeta_e = 0.2$ (Barnes et al. 2016). The nuclear heating rate that enters the macronova calculation is then

$$\dot{\epsilon}_{\text{heat}}(t) = f_{\text{tot}} [\dot{\epsilon}_\beta(t) + \dot{\epsilon}_\alpha(t) + \dot{\epsilon}_{\text{fis}}(t)]. \quad (11)$$

3 RESULTS

3.1 Nucleosynthesis

Unless mentioned otherwise, we refer to WinNet results with the FRDM mass model as a default. From our simulations we find an electron distribution reaching up to 0.3, but with the majority of matter being near 0.04. This results in a very robust r-process pattern up to and beyond the third, "platinum" r-process peak near $A = 195$, see right panel in Fig. 5. For the neutrino-wind models the picture is different: here the resulting abundance pattern is sensitive to the details and in particular to the electron fraction of a thermodynamic trajectory. Consequently, the resulting pattern varies strongly between different wind models. Due to their relative large electron fraction ($Y_e > 0.25$), none of them reaches substantially beyond nucleon numbers of $A = 130$.

An exhaustive comparison of nuclear network results is beyond the intention of this paper. Nevertheless, we perform a short comparison between the two networks (Winteler 2012; Mendoza-Temis et al. 2015) for one case (dynamic ejecta of run N4, NSNS binary with 1.2 and 1.4 M_\odot ; $t = 100$ days), simply in order to gauge by how much the nucleosynthesis results might be influenced by implementation details. In both cases we use the FRDM nuclear mass

model. The final mass fractions are shown in Fig. 6, left panel. The overall pattern agrees reasonably well, but there are noticeable differences in the regime from $A \approx 90$ to 170, due to the treatment of fission. We also briefly explore which impact the nuclear mass model has on the final abundance pattern (run N4; Mendoza-Temis network; right panel of Fig. 6). A major difference is the substantially higher mass fraction of trans-lead ($A > 207$) nuclei when DZ31 is used. Barnes et al. (2016) found that α -decays of these nuclei have a substantial impact on the late-time lightcurve, see below. Overall, the DZ31 model shows a closer agreement with the solar r-process pattern, especially around the third r-process peak ($A \approx 195$).

We also briefly compare the total nuclear energy generation rate resulting from both networks (each time using FRDM, for all dynamic ejecta) in Fig. 7. There is good agreement between both networks over many orders of magnitude, only at very late stages we find for some trajectories deviations of up to a factor of two. We leave more detailed comparisons of the effects of different input physics in the networks to future work.

3.2 Thermalization efficiency and nuclear heating rates

Since the various reaction products thermalize on different time scales, see Eq. (6)-(9), the nuclear mass model has also an impact on the total thermalization efficiencies. Since α -decays (due to translead nuclei) are enhanced, we find noticeable differences in the overall efficiencies, see Fig. 8. In all the cases f_{tot} remains approximately constant around ~ 0.7 , but decreases substantially slower at late times (for $t > 3$ days) for the DZ31 mass model⁴. Closely related, for DZ31 the net heating rate, Eq. (11), is significantly different, see Fig. 7, right panel: at late times ($t > 1$ day) it exceeds the FRDM-results by up to an order of magnitude. This has a serious impact on the resulting macronova lightcurves around the time of the peak emission.

3.3 Optical and near-IR macronova lightcurves

One of the major objectives of our work is to explore the detectability of macronovae using current and future wide field-of-view optical and near-IR facilities, either as a result of follow-up of LIGO triggers or through independent transient searches. Figures 9 and 10 show the expected optical and near-IR lightcurves in absolute magnitudes for the dynamical ejecta of our brightest NSNS (N5) and NSBH (B3) mergers, respectively. Each time, we show the results from our macronova model 1 ('MNmodel1'; see Sec. 2.4.2) and for model 2 ('MNmodel2'; see Sec. 2.4.3), once for the FRDM and once for the DZ31 nuclear mass model. Throughout this work we use LSST *grizy* filters and 2MASS *JHK* and magnitudes in the AB-system.

The dynamic ejecta in N5 has a mass ratio that deviates substantially from unity ($q = 0.78$), but is consistent with the currently known mass ratios of NSNS binaries. For example, the observed value of J0453+1559 is $q = 0.75$ (Martinez et al. 2015) and the recently discovered PSR J1913+1102 could have an even lower mass ratio (Lazarus et al. 2016). The left panel of Fig. 9 shows the results for the macronova model 1, the middle panel shows MNmodel2

⁴ Our results here differ somewhat from Barnes et al. (2016) in the sense that the ejecta are denser/slower. Therefore, the efficiencies can be higher in first few days and can actually increase if the α -decays do so.

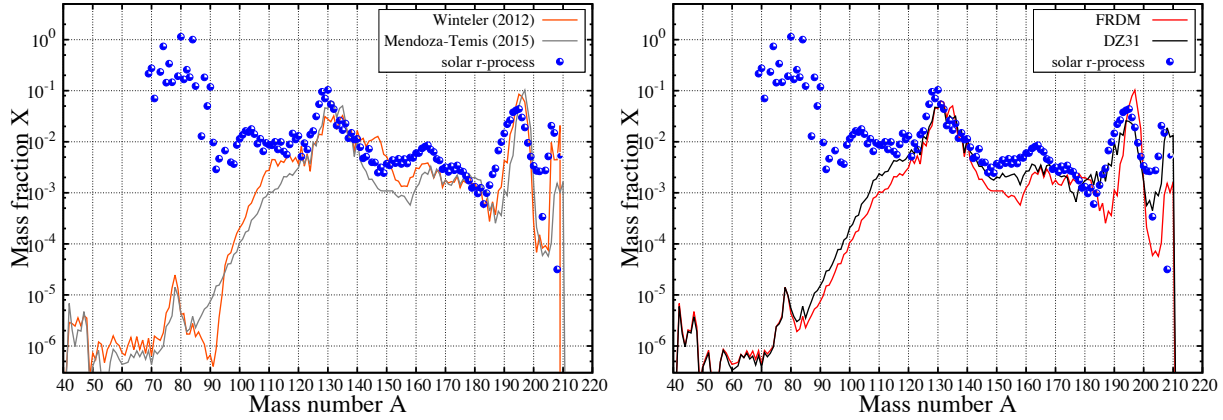


Figure 6. Left panel: comparison of the abundances for the run N4 (1.2 and $1.4 M_{\odot}$; $t = 100$ days) obtained with the nuclear reaction networks of Winteler (2012) and of Mendoza-Temis et al. (2015), both using the FRDM nuclear mass model. Right panel: comparison of the results for the FRDM and DZ31 nuclear mass model using the Mendoza-Temis et al. network. Note that the DZ31 mass formula is in much better agreement with the solar system abundances than FRDM, especially in the region around the “platinum peak” ($A \approx 195$).

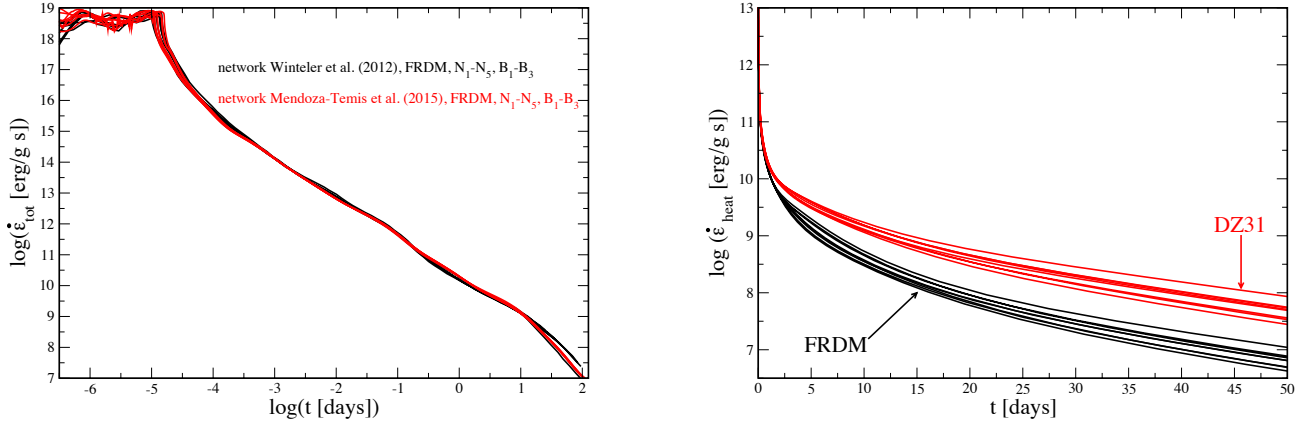


Figure 7. Left: Comparison of the total nuclear energy generation rates between the network of Winteler et al. (2012) and Mendoza-Temis et al. (2015), both using the FRDM mass model. The overall agreement between both networks is good over many orders of magnitude. Right: Net nuclear heating rates for the FRDM and DZ31 nuclear mass model (all runs N1-N5 and B1-B3; Mendoza-Temis et al. network). The DZ31 models yields consistently larger heating rates at late times ($t > 1$ day).

with the FRDM mass formula and the right panel refers to MNmodel2 with DZ31. The general trends with a fainter and faster lightcurve in the bluer bands is apparent, while the near-infrared (NIR) lightcurves can stay bright for several weeks. We typically have -11.5 at peak in the g band versus -13.8 in the K band. The MNmodel2 results are about 0.7 magnitudes brighter at peak, but decay faster at later times. Both effects are mainly due to the time variation of the thermalization efficiency, see Fig. 8. As expected from the enhanced net heating rate at late times (see Fig. 7)

the DZ31 mass model yields peak magnitudes that are another 0.8 magnitudes brighter than for the FRDM case. At the same time, both runs using MNmodel2 are significantly redder in the optical, being about one magnitude fainter at peak in the g band. Additionally, their g -band lightcurves peak much earlier – only half a day after the merger versus about three days for MNmodel1. Figure 10 shows the predictions for run B3 ($1.2 M_{\odot}$ NS and a $7.0 M_{\odot}$ BH with a dimensionless spin parameter $\chi = 0.9$). The BH mass of $7 M_{\odot}$ is close to the expected peak of the BH mass dis-

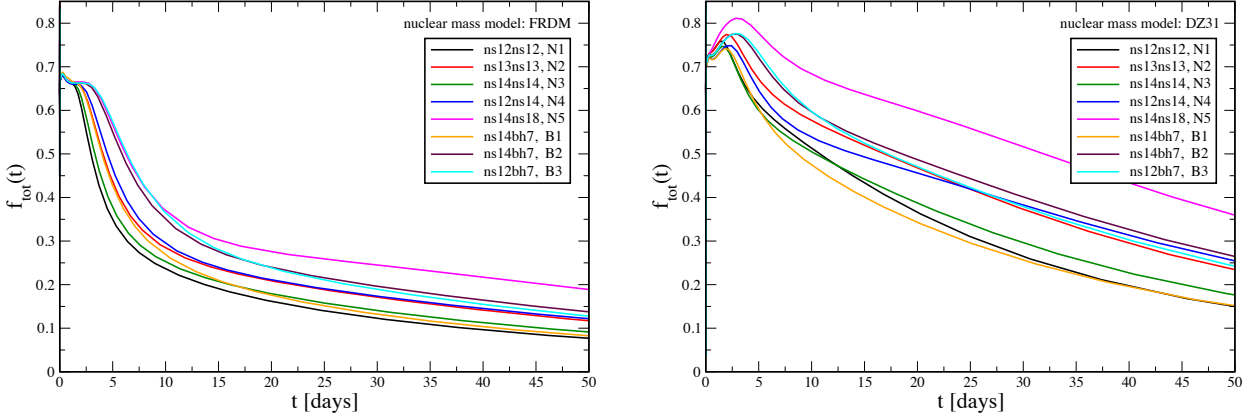


Figure 8. Thermalization efficiencies for the different nuclear mass models.

tribution (Özel et al. 2010), but the spin is admittedly high. However, if we are interested in NSBH systems that are able to launch a short GRB, we need a large BH spin ($\chi \approx 0.9$) in the first place in order to form an accretion torus. Otherwise the neutron star is essentially swallowed whole (see, for example, the discussion in Sec. 5.3 of Rosswog (2015c) and references therein) and no GRB can be launched. Moreover, measured BH spins in high-mass X-ray binary systems tend to have large spin values ($\chi > 0.85$), and these systems are the likely progenitors of NSBH binaries (McClintock et al. 2014).

In the most favorable NSBH case (MNmodel2, DZ31) a K -band peak magnitude brighter than -16 is reached. The g band reaches a similar brightness as for the NSNS case, but declines on a faster time scale for MNmodel1. Again, the objects are quite red, with the brightest magnitudes and more long lived light curves in the NIR. Figure 11 shows the lightcurves for selected wind models (MNmodel1). The parameters of the first shown model (wind3) are guided by the simulations of the neutrino-driven winds in the aftermath of a $1.4\text{-}1.4 M_{\odot}$ merger by Perego et al. (2014), where the central remnant survives for at least a few hundred milliseconds before collapsing into a BH. With only very few available wind simulations, we consider this for now as representative for neutrino-driven winds from a NSNS merger. We consider the parameters of the wind model shown in the second panel (wind4) as representative for unbound accretion disk material (Fernandez & Metzger 2013a; Just et al. 2015; Wu et al. 2016). The last shown wind model (wind9) is a rather extreme case where $0.1 M_{\odot}$ is ejected at $0.1c$, while still having a low opacity due to the large electron fraction ($Y_e = 0.25$; the lanthanide fraction in this case is $\sim 3.5 \times 10^{-5}$, see column six in Tab. 2).

For an efficient comparison, we have summarised the basic properties of the lightcurves for all models considered in Tab. 3. In addition to the peak magnitudes in LSST r and 2MASS J band, we calculated the time for which the lightcurve is within 1 magnitude of peak in those filters. All the calculated light curves available at: <http://snova.fysik.su.se/transient-rates/>.

3.4 Detection feasibility

Next, we estimate the expected number of observable macronovae by integrating the expected rate of neutron star mergers (NSMs) R_{NSM} over the comoving volume in which the resulting macronova is observable. The expected number of macronovae observable then becomes:

$$n_{\text{MN}} = \int_{z < z_{\text{max}}} R_{\text{NSM}} (1+z)^{-1} dV_C, \quad (12)$$

where dV_C is the comoving volume element and z_{max} is the maximum redshift at which the macronova is brighter than m_{lim} . For R_{NSM} we adopted an “informed best guess” value of $300 \text{ yr}^{-1} \text{ Gpc}^{-3}$, see Fig. 2. To study the detectability, the lightcurves in observer-frame $grizJHK$ were calculated from the time-dependent SEDs of each run using the Python package `snocosmo` (Barbary 2014) to account for spectral redshift. Calculations of cosmological distances and volumes were performed using the Python package `astrophy` (Astropy Collaboration et al. 2013). We assumed a cosmology with $H_0 = 67 \text{ km s}^{-1} \text{ Mpc}^{-1}$ and $\Omega_m = 0.307$ (Planck Collaboration et al. 2016).

The four panels in Figure 12 show representative model predictions for the expected number of MNe per year as a function of limiting AB magnitude over the whole sky, normalised to a nominal volumetric rate $R_{\text{NSM}} = 300 \text{ yr}^{-1} \text{ Gpc}^{-3}$ (left axis) and the corresponding reach in distance (axis on the right). Dashed lines at 75 Mpc and 140 Mpc show the quoted sensitivity limit for GW detections for LIGO run (Martynov et al. 2016; Abbott et al. 2016) for NSNS and NSBH respectively. We also indicate the limiting magnitudes of 60 and 180-second exposures for VISTA and LSST in J and K band and $grizy$, respectively. When determining the limiting magnitudes, we used the ESO Infrared Exposure Time Calculator⁵ for VISTA and a Python exposure time calculator for LSST⁶, assuming a target signal-to-noise ratio of 5. We also indicate the expected limiting magnitudes for the Zwicky Transient Facility (ZTF) $gri \sim 21$.

⁵ <https://www.eso.org/observing/etc/>

⁶ <https://github.com/lsst-sims/exposure-time-calc>

Lightcurve parameters					
run	r_{\max}	$\Delta t_{\text{mag}}(r)$	J_{\max}	$\Delta t_{\text{mag}}(J)$	comment
MNmodel1, FRDM					
ns12ns12 (N1)	-11.24	3.59	-12.75	6.34	
ns13ns13 (N2)	-11.31	4.64	-12.91	7.79	
ns14ns14 (N3)	-11.21	3.94	-12.72	6.80	
ns12ns14 (N4)	-11.48	5.49	-13.05	8.78	
ns14ns18 (N5)	-12.36	8.13	-13.64	11.59	
ns14bh7 (B1)	-11.21	2.46	-13.51	7.49	
ns14bh7 (B2)	-11.17	3.28	-13.62	9.26	
ns12bh7 (B3)	-11.40	2.65	-13.97	10.08	
wind1	-13.09	2.96	-13.24	5.60	
wind2	-13.11	4.14	-13.52	7.79	
wind3	-12.51	2.57	-12.80	4.47	
wind4	-13.51	6.66	-14.21	9.82	
wind5	-13.30	4.75	-13.73	8.40	
wind6	-13.50	4.96	-13.99	6.82	
wind7	-14.37	5.45	-15.17	8.46	
wind8	-13.60	11.02	-13.46	9.68	
wind9	-14.60	6.70	-15.50	9.62	
wind10	-13.44	2.89	-14.07	6.33	
wind11	-11.76	2.30	-14.09	5.43	$\kappa = 10 \text{ cm}^2/\text{g}$
wind12	-12.29	0.93	-14.26	3.63	$\kappa = 10 \text{ cm}^2/\text{g}$
wind13	-12.41	8.22	-12.41	11.02	
wind14	-13.33	5.27	-13.82	9.91	
wind15	-12.40	8.56	-12.44	10.93	
wind16	-13.36	5.77	-13.91	11.97	
wind17	-14.63	7.90	-15.67	10.95	
wind18	-11.34	5.51	-11.34	7.69	
wind19	-14.18	6.88	-13.91	12.30	
wind20	-15.08	4.56	-16.33	7.20	
wind21	-15.24	4.85	-16.23	7.77	
MNmodel2, FRDM					
ns12ns12 (N1)	-11.28	1.72	-12.97	3.71	
ns12ns14 (N4)	-11.31	2.18	-13.15	5.35	
ns13ns13 (N2)	-11.24	2.07	-13.06	4.87	
ns14ns14 (N3)	-11.23	1.87	-12.93	4.07	
ns14ns18 (N5)	-11.27	3.39	-13.65	6.85	
ns14bh7 (B1)	-11.69	1.55	-13.69	5.08	
ns14bh7 (B2)	-11.61	1.77	-13.79	6.67	
ns12bh7 (B3)	-11.78	1.42	-14.08	7.01	
MNmodel2, DZ31					
ns12ns12 (N1)	-11.65	3.30	-13.71	6.03	
ns12ns14 (N4)	-11.61	4.48	-13.95	7.49	
ns13ns13 (N2)	-11.67	4.59	-13.99	7.31	
ns14ns14 (N3)	-11.59	3.42	-13.64	6.22	
ns14ns18 (N5)	-11.77	6.63	-14.57	9.60	
ns14bh7 (B1)	-12.06	3.41	-14.53	7.66	
ns14bh7 (B2)	-12.04	5.60	-14.92	9.64	
ns12bh7 (B3)	-12.21	5.24	-15.29	10.30	
ns12bh7 (B3)	-8.32	0.22	-10.80	7.76	$\kappa = 100 \text{ cm}^2/\text{g}$

Table 3. Lightcurve parameters in LSST r and 2MASS J bands. r_{\max} and J_{\max} are the absolute AB-magnitude at maximum, Δt_{mag} is the time (in days), during which the lightcurve is within 1 magnitude of peak brightness. The dynamic ejecta for the NSNS and NSBH models have $\kappa = 10 \text{ cm}^2/\text{g}$ whereas the wind models have $\kappa = 1 \text{ cm}^2/\text{g}$ unless their lanthanide fraction should exceed a threshold value of $X_{\text{lan}} > 10^{-3}$. These few cases are indicated in the table. We also explore in one case (last line) the hypothetical possibility that the opacities of lanthanide-rich material should be substantially larger ($= 100 \text{ cm}^2/\text{g}$).

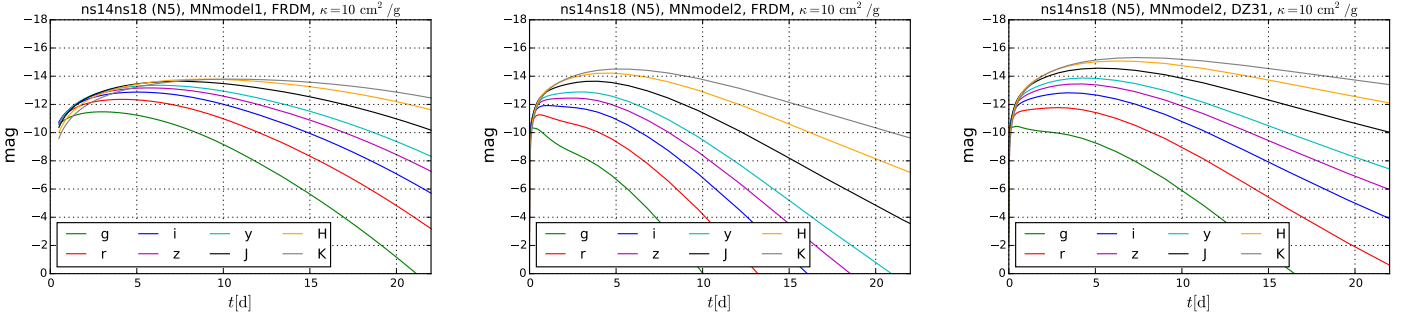


Figure 9. Comparison of the light curves in different bands for the dynamic ejecta of the brightest NSNS binary system (simulation N5; 1.4 and 1.8 M_{\odot}). The left panel shows the results for macronova model 1 (Grossman et al. (2014), fixed thermalization efficiency $f_{\text{tot}} = 0.5$), the other panels show the results for model 2 (time-dependent f_{tot}) with the FRDM nuclear mass model (middle) and the DZ31 nuclear mass formula (right). We could have used $m_{\text{ej,max}}$ here to set an upper limit but the mass dependence in Eq. (2) only has a minor impact on the peak magnitude.

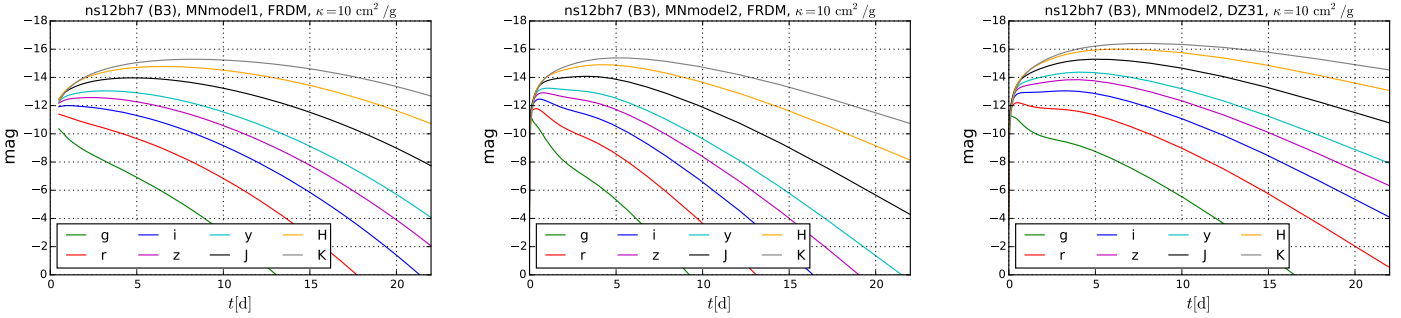


Figure 10. Comparison of the light curves in different bands for the dynamic ejecta of our brightest neutron star black hole system (simulation B3). The left panel shows the results for macronova model 1, the middle panel for model 2 with the FRDM nuclear mass model and the right panel shows the results of model 2 with the DZ31 nuclear mass formula.

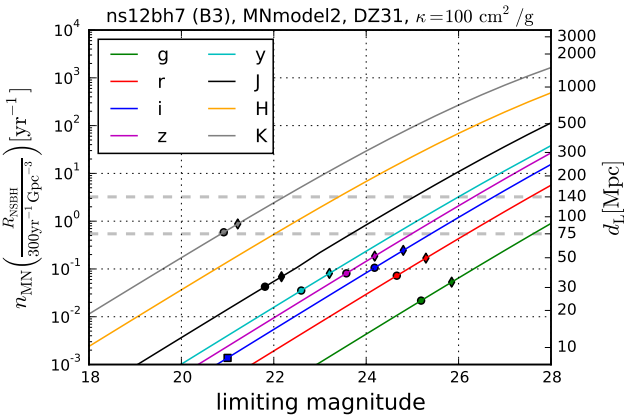


Figure 13. Expected number of MNe for the brightest NS-BH merger model (B3) and the hypothetical case that the effective opacity should be as large as $\kappa = 100 \text{ cm}^2/\text{g}$ (using the results from the DZ31 mass formula). The markers show the expected depths as in Fig. 12.

Here we have concentrated on a selection of the available models (N2, N5, B3 with DZ31 and wind20). Given the assumed rate of NSNS mergers, we can deduce the number of observable events for any given survey. We have done the calculations for these two given existing/upcoming facilities, but the community can use this for any of their fa-

vorite surveys. These calculations are also provided under <http://snova.fysik.su.se/transient-rates/>.

Figure 12 also allows to read off the relative efficiency to detect NSNS mergers in the different passbands. The lightcurves show that more flux is expected for longer wavelengths, indicating that near-IR surveys would be particularly suitable. However, given the difficulty for ground based instruments to observe at these wavelengths, it is reassuring that also optical telescopes have a good sensitivity for macronova detections. The figure shows that in this particular case, one minute exposures in the optical bands (i) can be as efficient in detecting the merger.

Fig. 12 is based on the best currently available opacity information. The opacities for dynamic ejecta, however, have just begun to be explored and are therefore not very accurately known. We therefore explore also the hypothetical case that the dynamic ejecta opacities should be as large as $100 \text{ cm}^2/\text{g}$, see Fig. 13. If such extreme opacities should be realized in nature, this would substantially deteriorate the detection prospect for the dynamic ejecta.

The above feasibility study shows that there are indeed prospects for finding optical and NIR emission from macronovae with large telescopes. More than a handful of events would be expected each year, distributed over the entire sky. In fact, if a survey such as LSST would allow high enough cadence (about once per night) in multiple filters, one could even discover macronovae without a trigger. Such un-triggered searches have already started, but are hampered by both difficulties in subtracting faint transients on potentially bright host galaxies, and by the background of supernovae (Doctor et al. 2016). The most interesting prospects for

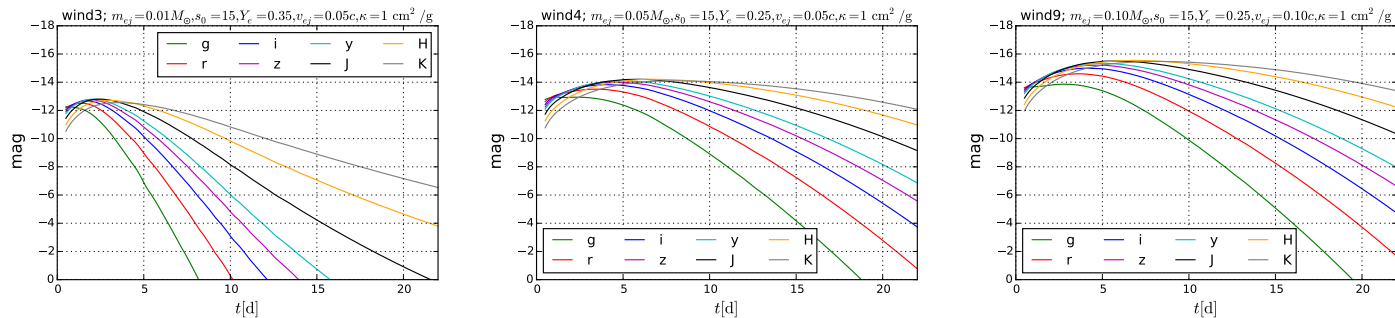


Figure 11. Lightcurves of selected wind models in different bands. The parameters of ‘wind3’ (left) are inspired by neutrino-driven winds in the aftermath of a NSNS merger, those of ‘wind4’ (middle) by unbound torus material (stages IV, VI and IX in Fig. 1) and ‘wind9’ is similar to ‘wind4’, but with slightly more optimistic parameters.

finding them clearly comes in connection with triggers from either GW signals or high-energy emission (Gamma-ray bursts).

3.5 Follow-up of LIGO triggers

The optical follow-up of gravitational wave signals is currently a large effort within the transient community (Abbott et al. 2016c). We can now relate our model predictions with ongoing surveys such as iPTF (Kasliwal et al. 2016) and Pan-STARRS (Smartt et al. 2016). These are typically conducted in the r band, reaching limiting magnitudes of $\sim 20 - 21$. This will be typical also for the upcoming very wide area search with ZTF. For the most recent GW signals, at a distance of 400 Mpc, the detectability is illustrated by Smartt et al. (2016, their Fig. 9).

To such large distances, none of our models for dynamical ejecta becomes bright enough to be detectable. Even the most optimistic wind models are below the detection threshold of Smartt et al. (2016) at these distances. However, note that the current LIGO configuration can detect NSNS mergers only out to 75 Mpc (Martynov et al. 2016). For such a distance, the wind model would be easily detected by the search such as that by Smartt et al. (2016), and also the more optimistic dynamical ejecta models (e.g., N5 MNmodel2 DZ31) could be detected by ZTF (Kasliwal et al. 2016) if nearby enough. With the rate of such events assumed above, we would expect about one such event per year, and not all may be observable by optical telescopes.

The larger telescopes studied here (LSST/VISTA) will more easily detect any such counterpart to a GW trigger, and as the sensitivity of LIGO for NSNS mergers increases from 75 to 200 Mpc, we will go from one event every second year to about 10 events per year, and these events would indeed be within range for these telescopes.

In this comparison we also note that the timescales for the brighter models is several days, and not the very steep declines envisioned by some groups (see for example Fig. 3 in Kasliwal et al. 2016, and our discussion in the introduction). This is of great importance in determining the observing strategy, and our models suggest that a nightly cadence would be suitable, with several nights needed to establish variability. On the other hand, pursuing the search for much more than 2 weeks, as in Smartt et al. (2016), seems not to be warranted by these models.

We thus conclude that forthcoming surveys with the 8-meter LSST (~ 10 sq. deg field of view) and existing 4-meter VISTA (~ 2 sq. deg) will be able to search for GW-EM counterparts for any expected trigger from LIGO involving at least one neutron star with

relatively short exposures per field. With such surveys, search areas of hundreds of sq. deg may be searched in a single night.

The feasibility of detection of coincident events is therefore promising. For more nearby mergers within ~ 30 Mpc, for most of the models considered also surveys like ZTF would have an excellent chance of capturing the lightcurves of macronovae in multiple filters.

3.6 GRB triggers for the macronova candidate

Another way to get a trigger for a macronova event is via high-energy emission. The best case for a macronova so far comes from (Tanvir et al. 2013). The detection of the short GRB 130603B is currently the best macronova candidate, the GRB had a fast decaying optical afterglow and was well placed within the host galaxy (de Ugarte Postigo et al. 2014) at redshift $z = 0.356$. The Hubble Space Telescope (HST) imaging of (Tanvir et al. 2013) detected an H -band candidate at 25.73 ± 0.20 (F160W) at 7 rest-frame days (9.5 in observer frame) past GRB. Simultaneous optical (F606W) observations did not detect the source down to 28.25 (95%).

Comparison to all models shows which ones are bright enough to explain this event as a macronova. In Fig. 15, upper panel, we display the magnitude in the mass-velocity plane (see bottom panel same figure) for MNmodel1 and FRDM (top) and MNmodel2 and DZ31 (bottom). The colors of the symbols indicate the magnitude difference with respect to the Tanvir et al. detection and thus show that several models are within a factor of 3 of the required luminosity (orange and red symbols). Therefore, if we interpret this event as a MN, we note that the opacities can not be very different from those used here. Even the otherwise most promising models (e.g. model B3) would not be able to account for these observations if the effective opacities should be as large as $\kappa = 100 \text{ cm}^2/\text{g}$.

The wind models provide sufficiently bright lightcurves for the macronovae. Most notably wind model 9 matches the H -band detection perfectly while model 7 is only ~ 0.5 mag too faint, which is not significant given the model uncertainties, see the right panel of Fig. 14. The parameters of these models are close to what is expected for unbound accretion torus material (see stage IV, VI and IX in Fig.1). The R -band upper limit, on the other hand, constrains the wind used for model 8, for which 27.81 is predicted. Perhaps even more interesting is that the brighter dynamical ejecta models also provide light curves that match this event, see left and middle panels of Fig. 14.

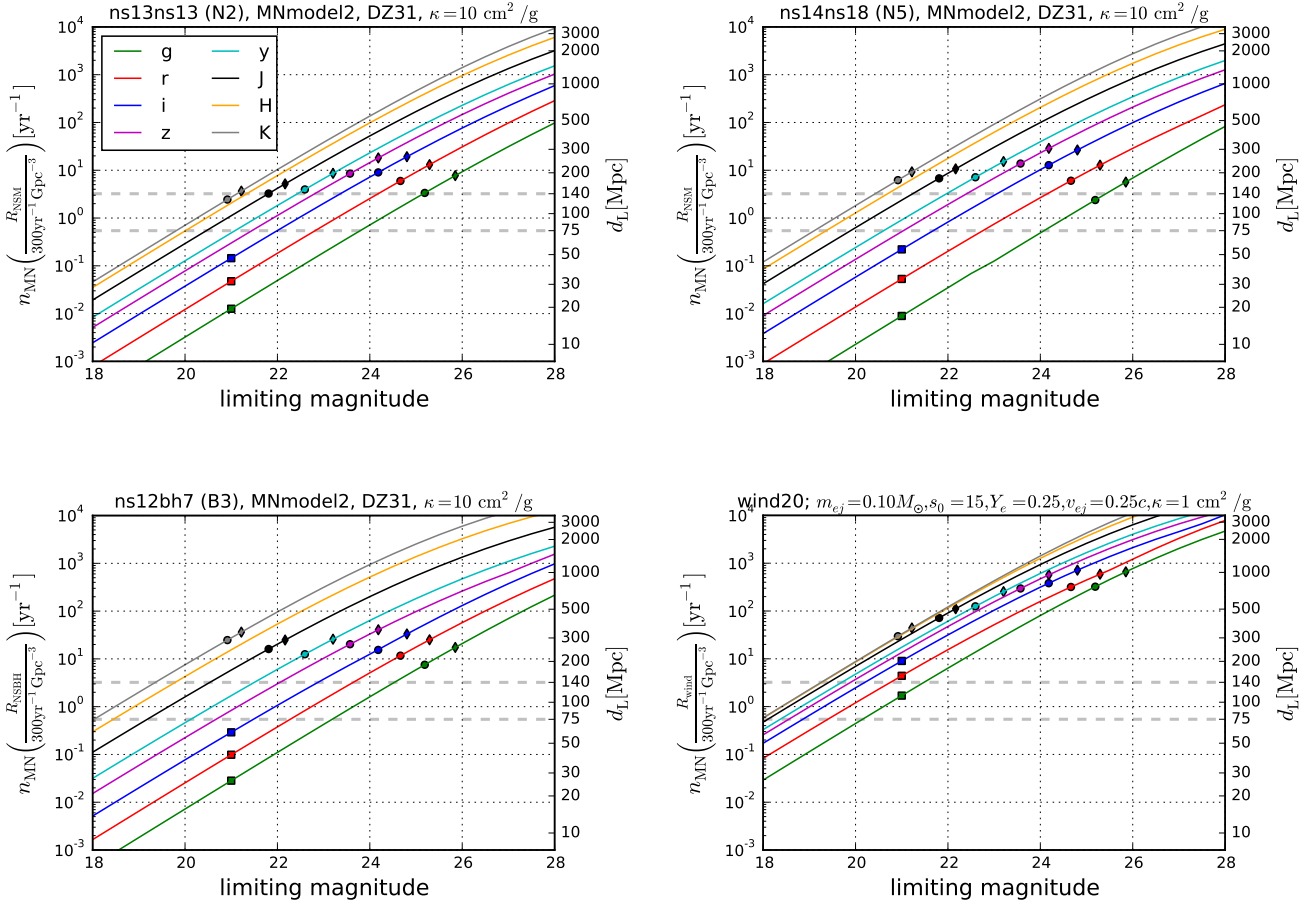


Figure 12. Expected number of MNe for selected bright models for each of the three categories (for the dynamic ejecta we use the brighter results coming from the DZ31 mass formula). The markers show the expected depths for a 60-second (circle) and 180-second (diamond) exposures with VISTA (*J&K* band) or LSST (*grizy*). Square markers show the expected numbers for a depth of 21 mag in *gri* as expected for ZTF. On the right-hand side the y-axis shows the luminosity distance up to which the NS merger rate was integrated to obtain n_{MN} . The gray dashed lines show the LIGO range for discoveries of gravitational wave signals from NS-NS mergers (75 Mpc) and NS-BH mergers (140 Mpc). Note that the results are scaled to the “best guess” for the NSNS merger rate of $300 \text{ yr}^{-1} \text{ Gpc}^{-3}$.

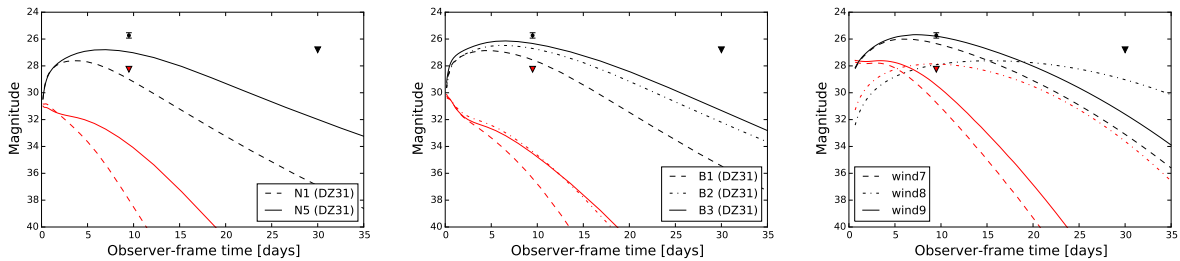


Figure 14. Lightcurves for selected models transformed to the redshift of GRB 130603B ($z = 0.356$) in HST-band F160W (black) and F606W (red). The down-pointing triangles correspond to 95% upper limits.

4 SUMMARY AND DISCUSSION

The major aim of this study was to explore the detectability of radioactively powered electromagnetic transients in the aftermath of compact binary mergers. We have performed simulations of neutron star mergers to extract hydrodynamic trajectories of the ejected material. These have been complemented by trajectories representing neutron star black hole mergers and various forms

of wind outflows that have been treated in a parametrized form. What we denote collectively as ‘winds’ can have different physical origins such as neutrino-driven outflows or the late-time release of accretion torus material.

Along these trajectories nuclear reaction network calculations were performed to extract the radioactive heating rates which, in turn, serve as input for the subsequent macronova modeling. We

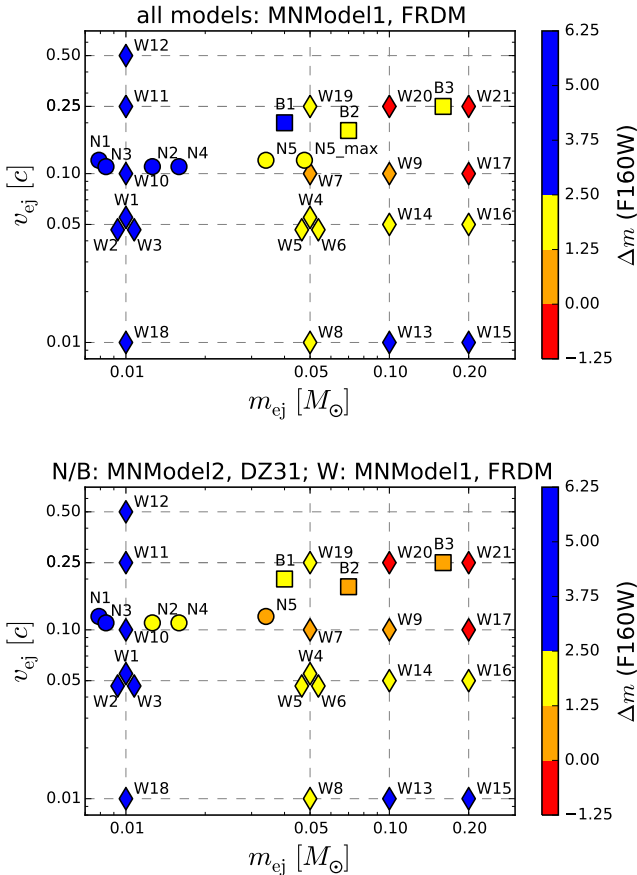


Figure 15. Comparison of our model predictions (same parameter space in $m_{\text{ej}} - v_{\text{ej}}$ as Fig. 4) with the H-band (F160W) observation in the aftermath of GRB 130603B (Tanvir et al. 2013). The wind models are shown as diamonds, NS-NS mergers as circles and NS-BH mergers as squares. Note that W1–3 and W4–6 correspond to models with the same mass and velocity, but with different electron fractions, see table 2. All wind models are calculated with MNmodel1 and FRDM, the dynamic ejecta results for NSNS mergers (labeled “N*”) and NSBH mergers (labeled “B*”) are once calculated with MNmodel1 and FRDM (upper panel) and once with MNmodel2 and DZ31 (lower panel).

have compared two different reaction networks (Winteler 2012; Mendoza-Temis et al. 2015) to ensure the robustness of our results. Since the r-process path for very neutron-rich ejecta meanders through a region of the nuclear chart where no experimental information is available such calculations are based on theoretical nuclear models. We have therefore explored the difference between two frequently used nuclear mass models, the Finite Range Droplet Model (FRDM) (Möller et al. 1995) and the 31-parameter model (DZ31) of Duflo & Zuker (1995). For the aspects explored in this manuscript the main differences for the observability come from different predictions for the amount of α -decaying trans-lead nuclei. We have further compared the results of two macronova models. The first one (Grossman et al. 2014) uses the FRDM mass model and assumes a fixed thermalization efficiency of 50%. In our second, and more sophisticated model, we use time-dependent thermalization efficiencies based on the recent work of Barnes et al. (2016) and we allow to switch between the FRDM and the DZ31 mass model. We have calculated the resulting macronova lightcurves in different bands for eight representative dynamic

ejecta cases, see Tab. 1, and for 21 wind models, see Tab. 2.

We find that the nuclear mass model has a decisive impact on the results. In terms of nucleosynthesis, the DZ31 model reproduces the solar-system r-process abundances around the platinum peak ($A=195$) with substantially higher accuracy than the FRDM model. It is worth emphasizing, however, that also other nuclear properties such as decay half-lives and fission yields have substantial uncertainties. With DZ31 one finds substantially larger amounts of trans-lead material and its α -decay yields nuclear heating rates that are, at the times relevant for the macronova emission, about an order of magnitude larger than in the FRDM case, see Fig. 7, right panel. In addition, the thermalization efficiencies in the DZ31 cases are increased by factors of a few. As a result, the DZ31 macronova light curves are substantially brighter than those obtained with FRDM.

We find that the more promising dynamic ejecta models from NSNS mergers reach K-band peak magnitudes in excess of -15 (model N5 with a mass ratio close to the observed NSNS binary J0453+1559; see right panel of Fig. 9), while the brightest NSBH dynamic ejecta model reaches values beyond -16 . The wind models with parameters inspired by neutrino-driven winds from an NSNS-merger peak below -13 , while models mimicking unbound torus matter (Just et al. 2015; Wu et al. 2016) reach peak values of -14 and $-$ with only slightly increased mass and velocity parameters – they can reach close to -16 (Fig. 11).

Since more flux is expected at longer wavelengths, near-IR surveys are particularly suitable for macronova detections. We note, however, that exposures in optical bands (i) may be as efficient in detecting such mergers. Since the transients are generally faint and other sources evolving on these time scales are abundant, the best detection chances come from events that are triggered by either GW-signals or GRB-emission. For our adopted “best guess merger rate” of $300 \text{ Gpc}^{-3} \text{ yr}^{-1}$ larger telescopes such as LSST or VISTA should detect of order 10 events per year. For mergers within 30 Mpc ZTF would have an excellent chance of capturing macronovae in multiple filters.

We also explored which of our models could be plausible explanations for the best-to-date macronova candidate, the transient observed in the aftermath of GRB 130603B (Tanvir et al. 2013; Berger et al. 2013). Adopting the DZ31 models as our standard, several of the explored cases get close to this observation. Both dynamic ejecta models (the non-equal mass NSNS merger model N5 and the NSBH models B2 and B3) and several of our wind models (wind7, wind9, wind17, wind20 and wind21) produce transients with similar properties. We note, however, that none of our dynamic ejecta models would be able to account for this observation, for the hypothetical case that the effective opacities would be substantially larger than our adopted value of $10 \text{ cm}^2/\text{g}$ (Kasen et al. 2013; Barnes & Kasen 2013; Tanaka & Hotokezaka 2013).

The results presented here are based on our currently best macronova models. These involve a chain of different calculations where each has its own challenges. For example, the calculations involve gravity, hydrodynamics, neutrino and nuclear reactions, thermalization efficiencies and an approximate treatment of radiation. For several of these ingredients there are substantial uncertainties, for example for the nuclear equation of the state, the nuclear physics near the neutron-dripline and the involved matter opacities. Moreover, we note that our current models are not using proper radiative transfer calculations. While the discussed results represent the current status of our models, they certainly can and

will be improved in future.

Lightcurves, expected rates and redshift distributions are available under: <http://snova.fysik.su.se/transient-rates/>.

ACKNOWLEDGEMENTS

It is a great pleasure to acknowledge stimulating discussions with many collaborators, in particular Almudena Arcones, Jennifer Barnes, Brian Metzger, Albino Perego and Friedrich-Karl Thielemann. This work has been supported by the Swedish Research Council (VR) under grant 621-2012-4870. It has further been supported by the CompStar network, COST Action MP1304, and by the Knut and Alice Wallenberg Foundation. MRW acknowledges support from the Villum Foundation (Project No. 13164) and the Danish National Research Foundation (DNRF91) and GMP was partly supported by the Deutsche Forschungsgemeinschaft through contract SFB 1245 and the BMBF-Verbundforschungsprojekt 05P15RDFN1. The simulations for this paper were performed on the facilities of the North-German Supercomputing Alliance (HLRN).

REFERENCES

- Abadie J., Abbott B. P., Abbott R., Abernathy M., Accadia T., Acernese F., Adams C., Adhikari R., Ajith P., Allen B., et al. 2010, *Classical and Quantum Gravity*, 27, 173001
- Abbott B. P., Abbott R., Abbott T. D., Abernathy M. R., Acernese F., Ackley K., Adams C., Adams T., Addesso P., Adhikari R. X., et al. 2016c, *Ap. J. Lett.*, , 826, L13
- Abbott B. P., Abbott R., Abbott T. D., Abernathy M. R., Acernese F., Ackley K., Adams C., Adams T., Addesso P., Adhikari R. X., et al. 2016a, *Physical Review Letters*, 116, 061102
- Abbott B. P., Abbott R., Abbott T. D., Abernathy M. R., Acernese F., Ackley K., Adams C., Adams T., Addesso P., Adhikari R. X., et al. 2016b, *arXiv:1607.07456*
- Abbott B. P., Collaboration L. S., Collaboration V., 2016, *Living Reviews in Relativity*, 19
- Antoniadis J., Freire P. C. C., Wex N., Tauris T. M., Verbiest J. P. W., Whelan D. G., 2013, *Science*, 340, 448
- Arnould M., Goriely S., Takahashi K., 2007, *Phys. Reports*, 450, 97
- Astropy Collaboration Robitaille T. P., Tollerud E. J., Greenfield P., Droettboom M., Bray E., Aldcroft T., Davis M., Ginsburg A., Price-Whelan A. M., Kerzendorf W. E., Conley A., Crighton N., et al. 2013, *Astron. & Astrophys.*, , 558, A33
- Audi G., Kondev F., Wang M., Pfeiffer B., Sun X., Blachot J., MacCormick M., 2012, *Chinese Physics C*, 36, 1157
- Barbary K., 2014
- Barnes J., Kasen D., 2013, *ApJ*, 775, 18
- Barnes J., Kasen D., Wu M.-R., Martinez-Pinedo G., 2016, *ApJ*, 829, 110
- Baumgarte T. W., Shapiro S. L., Shibata M., 2000, *ApJL*, 528, L29
- Bauswein A., Ardevol Pulpillo R., Janka H.-T., Goriely S., 2014, *ApJL*, 795, L9
- Bauswein A., Baumgarte T. W., Janka H.-T., 2013, *Physical Review Letters*, 111, 131101
- Bauswein A., Goriely S., Janka H.-T., 2013, *ApJ*, 773, 78
- Belczynski K., Repetto S., Holz D. E., O’Shaughnessy R., Bulik T., Berti E., Fryer C., Dominik M., 2016, *ApJ*, 819, 108
- Beloborodov A. M., 2008, in M. Axelsson ed., *American Institute of Physics Conference Series Vol. 1054 of American Institute of Physics Conference Series, Hyper-accreting black holes*. pp 51–70
- Berger E., Fong W., Chornock R., 2013, *ApJL*, 774, L23
- Bildsten L., Cutler C., 1992, *ApJ*, 400, 175
- Chruslinska M., Belczynski K., Bulik T., Gladysz W., 2016, *ArXiv e-prints*
- Cioffi R., Siegel D. M., 2015, *ApJL*, 798, L36
- de Ugarte Postigo A., Thöne C. C., Rowlinson A., Garcia-Benito R., Levan A. J., Gorosabel J., Goldoni P., Schulze S., Zafar T., Wiersema K., Sanchez-Ramirez R., Melandri A., D’Avanzo 2014, *Astron. & Astrophys.*, , 563, A62
- Deaton M. B., Duez M. D., Foucart F., O’Connor E., Ott C. D., Kidder L. E., Muhlberger C. D., Scheel M. A., Szilagy B., 2013, *ApJ*, 776, 47
- Demorest P. B., Pennucci T., Ransom S. M., Roberts M. S. E., Hessels J. W. T., 2010, *Nature*, 467, 1081
- Dessart L., Ott C. D., Burrows A., Rosswog S., Livne E., 2009, *ApJ*, 690, 1681
- Doctor Z., Kessler R., Chen H. Y., Farr B., Finley D. A., Foley R. J., Goldstein D. A., Wester W., 2016, *ArXiv e-prints*
- Duez M. D., Foucart F., Kidder L. E., Ott C. D., Teukolsky S. A., 2010, *Classical and Quantum Gravity*, 27, 114106
- Duflo J., Zuker A. P., 1995, *Phys. Rev. C*, 52, R23
- Eichler D., Livio M., Piran T., Schramm D. N., 1989, *Nature*, 340, 126
- Eichler M., Arcones A., Kelic A., Korobkin O., Langanke K., Marketin T., Martinez-Pinedo G., Panov I., Rauscher T., Rosswog S., Winteler C., Zinner N. T., Thielemann F.-K., 2015, *ApJ*, 808, 30
- Fernandez R., Metzger B. D., 2013a, *MNRAS*, 435, 502
- Fernandez R., Metzger B. D., 2013b, *ApJ*, 763, 108
- Fernandez R., Metzger B. D., 2015, *ArXiv e-prints*
- Fernandez R., Quataert E., Schwab J., Kasen D., Rosswog S., 2015, *MNRAS*, 449, 390
- Fontes C. J., Fryer C. L., Hungerford A. L., Hakel P., Colgan J., Kilcrease D. P., Sherrill M. E., 2015, *High Energy Density Physics*, 16, 53
- Foucart F., 2012, *Phys. Rev. D*, 86, 124007
- Foucart F., Deaton M. B., Duez M. D., Kidder L. E., MacDonald I., Ott C. D., Pfeiffer H. P., Scheel M. A., Szilagy B., Teukolsky S. A., 2013, *Phys. Rev. D*, 87, 084006
- Foucart F., Deaton M. B., Duez M. D., O’Connor E., Ott C. D., Haas R., Kidder L. E., Pfeiffer H. P., Scheel M. A., Szilagy B., 2014, *Phys. Rev. D*, 90, 024026
- Freiburghaus C., Rosswog S., Thielemann F.-K., 1999, *ApJ*, 525, L121
- Fuller G. M., Fowler W. A., Newman M. J., 1982, *ApJS*, 48, 279
- Giacomazzo B., Perna R., Rezzolla L., Troja E., Lazzati D., 2013, *ApJL*, 762, L18
- Gondek-Rosinska D., Kowalska I., Villain L., Ansorg M., Kucaba M., 2016, *ArXiv e-prints*
- Goriely S., 2015, *European Physical Journal A*, 51, 22
- Grossman D., Korobkin O., Rosswog S., Piran T., 2014, *MNRAS*, 439, 757
- Hotokezaka K., Kiuchi K., Kyutoku K., Muranushi T., Sekiguchi Y.-i., Shibata M., Taniguchi K., 2013, *Phys. Rev. D*, 88, 044026
- Hotokezaka K., Kiuchi K., Kyutoku K., Okawa H., Sekiguchi Y.-i., Shibata M., Taniguchi K., 2013, *Phys. Rev. D*, 87, 024001

- Hotokezaka K., Kyutoku K., Okawa H., Shibata M., Kiuchi K., 2011, *Phys. Rev. D*, 83, 124008
- Hotokezaka K., Wanajo S., Tanaka M., Bamba A., Terada Y., Piran T., 2016, *MNRAS*, 459, 35
- Jin Z.-P., Li X., Cano Z., Covino S., Fan Y.-Z., Wei D.-M., 2015, *ApJL*, 811, L22
- Just O., Bauswein A., Pulpillo R. A., Goriely S., Janka H.-T., 2015, *MNRAS*, 448, 541
- Kaplan J. D., Ott C. D., O'Connor E. P., Kiuchi K., Roberts L., Duez M., 2014, *ApJ*, 790, 19
- Kasen D., Badnell N. R., Barnes J., 2013, *ApJ*, 774, 25
- Kasliwal M. M., Cenko S. B., Singer L. P., Corsi A., Cao Y., Barlow T., Bhalerao V., Bellm E., Cook D., Duggan G. E., Ferretti R., Frail D. A., et al., 2016, *ApJL*, 824, L24
- Kastaun W., Galeazzi F., 2015, *Phys. Rev. D*, 91, 064027
- Kochanek C. S., 1992, *ApJ*, 398, 234
- Kodama T., Takahashi K., 1975, *Nuclear Physics A*, 239, 489
- Korobkin O., Rosswog S., Arcones A., Winteler C., 2012, *MNRAS*, 426, 1940
- Kulkarni S. R., 2005, *ArXiv Astrophysics e-prints*
- Kyutoku K., Ioka K., Shibata M., 2013, *Phys. Rev. D*, 88, 041503
- Langanke K., Martinez-Pinedo G., 2001, *Atomic Data and Nuclear Data Tables*, 79, 1
- Lattimer J. M., Schramm D. N., 1974, *ApJ*, (Letters), 192, L145
- Lazarus P., Freire P. C. C., Allen B., Aulbert C., Zhu W. W., 2016, *ApJ*, 831, 150
- Lehner L., Liebling S. L., Palenzuela C., Caballero O. L., O'Connor E., Anderson M., Neilsen D., 2016, *Classical and Quantum Gravity*, 33, 184002
- Li L.-X., Paczyński B., 1998, *ApJL*, 507, L59
- Martin D., Perego A., Arcones A., Thielemann F.-K., Korobkin O., Rosswog S., 2015, *ApJ*, 813, 2
- Martinez J. G., Stovall K., Freire P. C. C., Deneva J. S., Jenet F. A., McLaughlin M. A., Bagchi M., Bates S. D., Ridolfi A., 2015, *ApJ*, 812, 143
- Martynov D. V., Hall E. D., Abbott B. P., Abbott R., Abbott T. D., Adams C., Adhikari R. X., Anderson R. A., Anderson S. B., Arai K., et al. 2016, *Phys. Rev. D*, 93, 112004
- McClintock J. E., Narayan R., Steiner J. F., 2014, *Space Science Review*, 183, 295
- McMillan P. J., 2011, *MNRAS*, 414, 2446
- Mendoza-Temis J., Martinez-Pinedo G., Langanke K., Bauswein A., Janka H.-T., 2015, *Phys. Rev. C*, 92, 055805
- Metzger B. D., 2016, *ArXiv e-prints*
- Metzger B. D., Bauswein A., Goriely S., Kasen D., 2015, *MNRAS*, 446, 1115
- Metzger B. D., Berger E., 2012, *ApJ*, 746, 48
- Metzger B. D., Martinez-Pinedo G., Darbha S., Quataert E., Arcones A., Kasen D., Thomas R., Nugent P., Panov I. V., Zinner N. T., 2010, *MNRAS*, 406, 2650
- Metzger B. D., Piro A. L., Quataert E., 2008, *MNRAS*, 390, 781
- Möller P., Nix J. R., Myers W. D., Swiatecki W. J., 1995, *At. Data Nucl. Data Tables*, 59, 185
- Moller P., Pfeiffer B., Kratz K.-L., 2003, *Phys. Rev.*, C67, 055802
- Monaghan J. J., 2005, *Reports on Progress in Physics*, 68, 1703
- Mumpower M. R., Surman R., McLaughlin G. C., Aprahamian A., 2016, *Progress in Particle and Nuclear Physics*, 86, 86
- Murguia-Berthier A., Montes G., Ramirez-Ruiz E., De Colle F., Lee W. H., 2014, *ApJL*, 788, L8
- Murguia-Berthier A., Ramirez-Ruiz E., Montes G., De Colle F., Rezzolla L., Rosswog S., Takami K., Perego A., Lee W. H., 2016, *ArXiv e-prints*
- Oechslin R., Janka H., Marek A., 2007, *A & A*, 467, 395
- Özel F., Psaltis D., Narayan R., McClintock J. E., 2010, *ApJ*, 725, 1918
- Panov I. V., Kolbe E., Pfeiffer B., Rauscher T., Kratz K.-L., Thielemann F.-K., 2005, *Nuclear Physics A*, 747, 633
- Panov I. V., Korneev I. Y., Rauscher T., Martinez-Pinedo G., Kelić-Heil A., Zinner N. T., Thielemann F.-K., 2010, *A & A*, 513, A61
- Perego A., Rosswog S., Cabezón R. M., Korobkin O., Käppeli R., Arcones A., Liebendörfer M., 2014, *MNRAS*, 443, 3134
- Petermann I., Langanke K., Martinez-Pinedo G., Panov I. V., Reinhard P. G., Thielemann F. K., 2012, *Eur. Phys. J.*, A48, 122
- Petrillo C., Dietz A., Cavaglia M., 2013, *ApJ*, 767, 140
- Planck Collaboration Ade P. A. R., Aghanim N., Arnaud M., Ashdown M., Aumont J., Baccigalupi C., Banday A. J., Barreiro R. B., Bartlett J. G., et al. 2016, *Astron. & Astrophys.*, 594, A13
- Price D. J., 2012, *Journal of Computational Physics*, 231, 759
- Radice D., Galeazzi F., Lippuner J., Roberts L. F., Ott C. D., Rezzolla L., 2016, *Mon. not. RAS.*, 460, 3255
- Rauscher T., Thielemann F.-K., 2000, *Atomic Data and Nuclear Data Tables*, 75, 1
- Roberts L. F., Kasen D., Lee W. H., Ramirez-Ruiz E., 2011, *ApJL*, 736, L21
- Rosswog S., 2005, *ApJ*, 634, 1202
- Rosswog S., 2009, *New Astronomy Reviews*, 53, 78
- Rosswog S., 2013, *Royal Society of London Philosophical Transactions Series A*, 371, 20272
- Rosswog S., 2015a, *MNRAS*, 448, 3628
- Rosswog S., 2015b, *Living Reviews of Computational Astrophysics* (2015), 1
- Rosswog S., 2015c, *International Journal of Modern Physics D*, 24, 1530012
- Rosswog S., Liebendörfer M., 2003, *MNRAS*, 342, 673
- Rosswog S., Liebendörfer M., Thielemann F.-K., Davies M., Benz W., Piran T., 1999, *A & A*, 341, 499
- Rosswog S., Piran T., Nakar E., 2013, *MNRAS*, 430, 2585
- Ruffert M., Janka H.-T., 2001, *A&A*, 380, 544
- Schaback R., Wendland H., 2006, *Acta Numer.*, 15, 543
- Shen H., Toki H., Oyamatsu K., Sumiyoshi K., 1998, *Nuclear Physics A*, 637, 435
- Shibata M., Taniguchi K., 2006, *Phys. Rev. D*, 73, 064027
- Siegel D. M., Ciolfi R., Rezzolla L., 2014, *ApJL*, 785, L6
- Smartt S. J., Chambers K. C., Smith K. W., Huber M. E., Young D. R., Cappellaro E., Wright D. E., Coughlin M., Schultz A. S. B., Denneau L., Flewelling H., Heinze A., et al., 2016, *MNRAS*, 462, 4094
- Smartt S. J., Chambers K. C., Smith K. W., Huber M. E., Young D. R., Cappellaro E., Wright D. E., et al., 2016, *MNRAS*, 462, 4094
- Springel V., 2010, *ARAA*, 48, 391
- Takami K., Rezzolla L., Baiotti L., 2014, *ArXiv e-prints*
- Tanaka M., Hotokezaka K., 2013, *ApJ*, 775, 113
- Tanvir N. R., Levan A. J., Fruchter A. S., Hjorth J., Hounsell R. A., Wiersema K., Tunnicliffe R. L., 2013, *Nature*, 500, 547
- Thielemann F.-K., Arcones A., Käppeli R., Liebendörfer M., Rauscher T., Winteler C., Fröhlich C., Dillmann I., Fischer T., Martinez-Pinedo G., Langanke K., Farouqi K., Kratz K.-L., Panov I., Korneev I. K., 2011, *Progress in Particle and Nuclear Physics*, 66, 346
- Timmes F. X., Swesty F. D., 2000, *ApJS*, 126, 501
- Wanajo S., Janka H.-T., 2012, *ApJ*, 746, 180

- Wanajo S., Sekiguchi Y., Nishimura N., Kiuchi K., Kyutoku K., Shibata M., 2014, *ApJL*, 789, L39
- Wang M., Audi G., Wapstra A., Kondev F., MacCormick M., Xu X., Pfeiffer B., 2012, *Chinese Physics C*, 36, 1603
- Wendland H., 1995, *Advances in Computational Mathematics*, 4, 389
- Winteler C., 2012, PhD thesis, University Basel, CH
- Winteler C., Käppeli R., Perego A., Arcones A., Vasset N., Nishimura N., Liebendörfer M., Thielemann F.-K., 2012, *ApJL*, 750, L22
- Wu M.-R., Fernandez R., Martinez-Pinedo G., Metzger B. D., 2016, *MNRAS*
- Yang B., Jin Z.-P., Li X., Covino S., Zheng X.-Z., Hotokezaka K., Fan Y.-Z., Piran T., Wei D.-M., 2015, *Nature Communications*, 6, 7323
- Zinner N. T., 2007, PhD Thesis, University of Aarhus